UNIVERSITÁ DEGLI STUDI DI PADOVA

DIPARTIMENTO DI INGEGNERIA INDUSTRIALE

CORSO DI LAUREA IN INGEGNERIA AEROSPAZIALE

Tesi di Laurea Magistrale

CFD study on the effect of a transonic fan downstream of an S-shape duct

Supervisor Ch.mo Prof. Benini Ernesto
Supervisor Dr. Kipouros Timoleon
Supervisor Prof. Savill Mark

Laureando: Marco Tridente

ANNO ACCADEMICO 2018 - 2019

Contents

List of Figures

List of Tables

Nomenclature

PR	=	Pressure Ratio
η	=	Isentropic Efficiency
LE	=	Leading Edge
TE	=	Trailing Edge
PS	=	Pressure Side
SS	=	Suction Side
BL	=	Boundary Layer
BLI	=	Boundary Layer Ingesting
DP	=	Distributed Propulsion
r	=	Radius
P_i^0	=	Total Pressure Inlet
cp	=	Pressure Recovery Factor

Abstract

Il lavoro condotto durante questi quattro mesi preso l'Universitá di Cranfield incentrato sul capire ed analizzare quale interazione puó nascere quando a valle di una presa dinamica a S viene posto un fan transonico. In questo studio, il fan transonico viene fornito dalla NASA ed é il test case R67, mentre per la S-duct la geometria baseline di Delot é stata presa in considerazione. Prima di eseguire la simulazione completa, alcuni step preliminari sono stati eseguiti:

- Simulazione del singolo canale con diverse tipologie di mesh
- Simulazione del full annulus
- Simulazione della S-duct con fan transonico a valle

Inoltre, deve essere specificato che la geometria della presa dinamica é stata adattata da Dal Magro in [12], nel cui lavoro, di comune accordo si é deciso di procedere a due diverse ottimizzazioni della S-duct, per cercare di ridurre il livello di distorsione che si veniva a creare. I risultati di tali simulazioni con il confronto baseline e geometrie ottimizzate sono presentati nella parte conclusiva della tesi.

Introduction

The MSc thesis has been carried out at Cranfield University (UK) in accordance with the guidelines provided by professor Benini Ernesto of University of Padua. The overall research work, lasted almost 5 months, aims to preliminarly analyze the interaction between an S-duct intake and a transonic fan. As a matter of fact, the fan that is taken into consideration for the study is the isolated rotor R67 developed by NASA, which has already been studied throughout the years. Despite of this fact, few are the works in which the fan is placed immediately after an S-shape intake; an example of this type of research is done by Paul G. Tucker in [24]. The first step required for the work was the reconstruction of the blade of the fan, using the TurboGrid ANSYS' tool in which the mesh of the model has been implemented as well. Consequently, the model should have been validated by comparing it with the experimental data; the simulations are thought in order to describe all the compressor map. In order to make it possible, six different speedlines are studied to understand the behaviour of the rotor at different rotational speed. Every speedline has the peculiarity that the rotational velocity is constant, whilst the outlet's pressure is varied from the choking condition (vertical asymptote) to the stall margin. All of these simulation are concerned with the single channel (only one blade was simulated) and the flowfield at the inlet is not affected by any deviation; the so-called clean flow. For these CFD calculation the Cranfield University Delta's cluster was exploited, which allowed the use of 16 CPU for each simulation. The first challenging step was the setting of the parameters needed for the simulation of the full annulus. Before doing that, the geometry needed to be modified since the central part of the shaft was left blank along the revolution of the 22 blades of the rotor. Therefore, by knowing the geometrical data of hub and shroud, an ogive was modeled in SolidWorks and then placed upstream of the rotor. For this computational analysis 16 CPU are used but the computational cost has highly risen, since the number of the nodes has become 22 times the initial ones. Despite the high time-demanding the full annulus compressor map was carried out either for the 100% of the rotational speed or for the 95%. As it is discussed along the thesis, this is due to the fact of the perfect match between the fan and the S-duct at those conditions. As it is concerned with the S-duct intake the baseline studied by Delot is taken into consideration. The problem is the fact that the geometry was not compatible, and therefore, it was adapted to the geometrical requirement of the fan in [12]. Consequently, another diversity between the two component has been solved; this was related to the inlet condition of the intake which must satisfied the inlet condition of the fan. This problem was also carried out in [12], by varying the initial condition in order to match the inlet pressure of the fan. In order to do so, a parametric study was

implemented in [12], to work out the perfect P_i^0 to gain the right average pressure for the rotor. Once the geometry and the all the overall conditions were reached, the two components were assembled in CFX-Pre and the speed line at 95% of the rotational speed was calculated. In addition, a comparison with the clean flow at inlet is drawn to quantify the losses in efficiency due to the distorted flow coming from the intake. Moreover, in agreement with the author of [12], it was decided to start a process of optimization for the intake. As a matter of fact, the objective function selected are the pressure recovery factor (*cp*) and the DC60, which measures the engine face distortion. The results were lately compared with the ones of the baseline geometry. Finally, another optimization process was decided with [12], but the objective were different; for instance the *cp* was object of minimization, but the other one is the swirl angle. The last step was the understanding of which of the parameters (between swirl and DC60) affected more the overall performance of the fan.

Chapter 1

State-of-the-art review

A propulsive system is defined as a mean by which a body is given the thrust. Despite of this fact, the engines are divided into two families; as a matter of fact both air-breathing and rockets exist. The main difference is how the thrust occurs; in fact, in the former ones the fluid is firstly breathed in from the outside and then, once accelerated, released by the nozzle, whilst in the latter ones the fluid is initially stored inside and then exhausted. Therefore, in the aeronautic propulsion the air-breathing engine is used and, of course, it is characterized by different features. Nowadays, the most common and efficient propulsive system is the turbofan, in which a fan is placed upstream of the compressor in order to suck in more air. Before proceeding it is significant to know all the components of which an engine consists of. The first part that the fluid encounters is the intake, which has the duty to drive the air to the compressor as either uniform or stable as possible by increasing its static pressure. After that, the compressor should provide the right compression to bring the fluid to the combustion chamber, in which there is the injection of the fuel to make the combustion happens. Now, the fluid passes through the turbine to reach the nozzle by which it is exhausted.

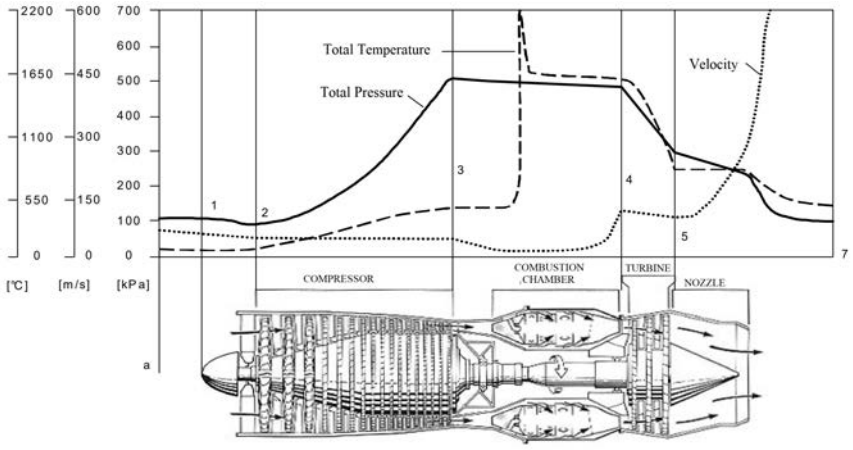

Figure 1: Properties variation inside a turbojet

The previous figure shows how the properties vary inside an aircraft engine (in this case a turbojet), but, since the main purpose of this work is the analisys of a fan it might be interesting to focus more on the turbofan. This is similar to the turbojet, except for the fact that part of the energy of the turbine is used to move a fan upstream

the compressor, instead of producing thrust in the nozzle. Doing so, the mass flow breathed in increases bringing about a reduction in the specific thrust; moreover the most significant aspect is that in a turbofan the propulsive efficiency is increased.
It is now the moment to focus on the features of a compressor, and, especially on the difference between a subsonic and a transonic one.

1.1 Axial Compressors

As briefly analyzed before, the compressor must increase the pressure of the fluid untill the optimal value for the combustion chamber. Nowadays, mostly in the entire aircraft propulsion the axial compressor is used due to its ability on working with large mass flow and the high efficiency (i.e. 3-5% more than the centrifugal compressor). The incoming airflow is axial, which means that it is parallel to the axis of rotation.

Moreover, it consists of multiple stages - these are based on two rows of blades. The first one that encounters the incoming fluid is the rotor, which is the moving part of the compressor and it is connected to the central shaft; after it there is the stator, that, as it is stated by the name, is fixed and does not rotate. Its main duty is to transform the kinectic energy into static pressure through diffusion and to straighten up the direction of the flow; these two rows of blade together form a stage. In the following figure all of these features are depicted.

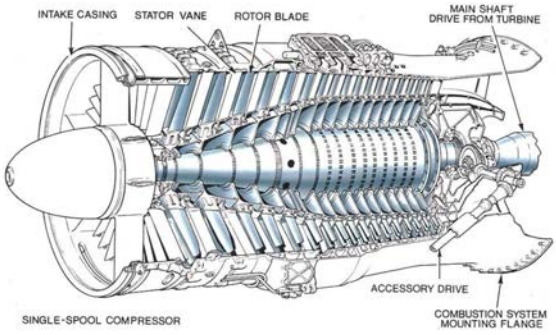

Figure 2: Longitudinal section of single spool axial compressor

Sometimes the use of more stator blades is possible, in fact, downstream of the last stage OGV (outlet guided vanes) might be provided for two different reasons:

1. Structural function for the shell of the engine
2. Reduction of the swirl of the fluid before it enters in the channel for the combustion chamber

Moreover, even at the inlet of the compressor the usage of stator vanes (IGV) is common in order to reduce the relative Mach. As a matter of fact, by using them, the

velocity is deflected, taking costant the axial component and decreasing the relative one. Furthemore the stacking angle is controlled and varied to improve the off design performance of the compressor [6]. All of these solution are usually considered whenever the number of the stages is more than 5.

1.1.1 Triangles of Velocities

The triangles of velocities are generally drawn either to represent the properties of the fluid through the rotor in its system of reference (relative frame) or to understand how the energy is exchanged within a stage. From now on, the inlet is marked as number 1, the outlet of the rotor as number 2 and the exit of the stage (outlet of the stator) as number 3, the behaviour of the velocities is shown in Fig. 3.

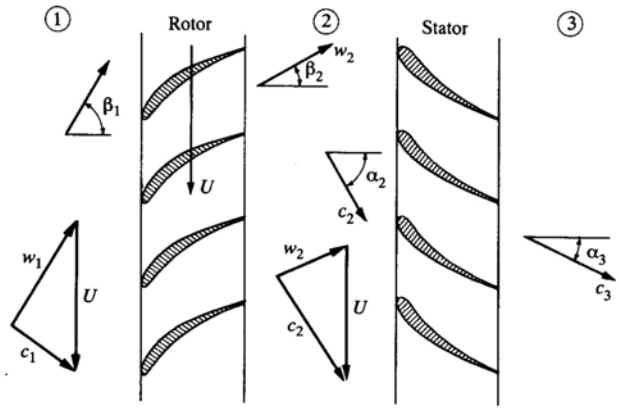

Figure 3: Triangle of velocities of an axial compressor (cit. Hill-Peterson)

The velocities taken into considerations are:

- c, absolute flow velocty
- w, relative flow velocity
- U, tangential blade speed ($U = \omega \wedge r$)

and the relation that exists is

$$\vec{c} = \vec{w} + \vec{U} \tag{1}$$

The Fig. 3 is referred to the mean radius of the compressor, but, as well as for all the sections of the blade the properties vary similarly. Through the rotor the mechanic energy of the shaft is transformed into fluid enthalpy [6], by bringing about the increase of absolute velocity, static and total temperature. Therefore, as the absolute velocity increases, the relative velocity must decrease to satisfy the equation 1 and as a consequence of that the static pressure increases. On the other hand, in the stator

blade the total temperature is conserved as the entire work of the stage is done by the rotor, and they are a diffuser for the absolute velocity. Consequently, there is only a loss of total pressure due to the friction of the fluid with the blade.

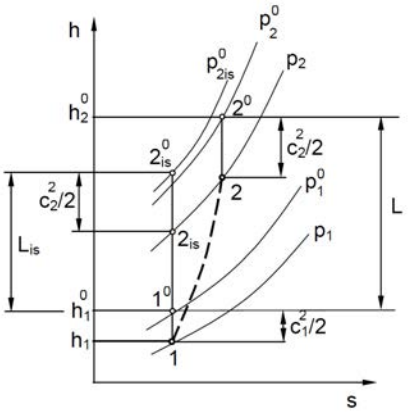

Figure 4: Termodynamic properties throughout a compression process

1.1.2 Isentropic Efficiency

The compression process throughout the compressor should be done with the higher efficiency possible, which brings about the less absorption of mechanical energy provided by the shaft [6]. This phenomenon is described from the isentropic efficiency, that is quantified (referring to the compression process of figure 4) as:

$$\eta_{is} = \frac{L_{is}}{L} = \frac{h_{2is}^0 - h_1^0}{h_2^0 - h_1^0} \tag{2}$$

The so defined efficiency in equation 2 is called total-to-total efficiency. As a matter of fact there are two ways to describe this property; the former one is the one previously analyzed, whilst the second one is the so-called total-to-static efficiency. What is changing, mathematically speaking, is the use of the static enthalpy instead of the total one at the exit. This fact is easily explained: take into consideration the entire compressor or at least, the last stage, in which the kinetic load is not converted into work or as it is said, it is lost, there is no sense to use the total status for the definition of the efficiency.

1.1.3 Polytropic Efficiency

The isentropic efficiency, however, is not able to describe faithfully how well the machine works, due to its dependency from the pressure ratio. Therefore, the efficiency developed previously decreases as the $\triangle h^0$ increases. In fact, by looking at Fig. 4,

the higher the exit temperature is, the higher the real work is and, since it is at the denominator of equation 2, the lower the efficiency is. To avoid this problem, another pressure-ratio indipendent parameter has been studied: the polytropic efficiency. This is defined as the isentropic efficiency of a termodynamic adiabatic process in which the initial and final pressure present an infinitesimal difference as shown in the following figure.

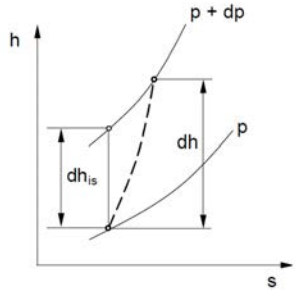

Figure 5: Definition of polytropic efficiency

From the previous image the polytropic efficiency is defined as:

$$\eta_{pol} = \frac{dh_{is}}{dh} = \frac{dp/\rho}{c_p dT} \tag{3}$$

which can be easily written in the most-known expression of η_{pol}:

$$\eta_{pol} = \frac{k-1}{k} \frac{ln(\frac{p_2^0}{p_1^0})}{ln(\frac{T_2^0}{T_1^0})} \tag{4}$$

1.1.4 Compressor map

The compressor map is an essential chart by which it is possible to understand how the machine works in terms of mass flow rate, pressure ratio and efficiency. Immediately,

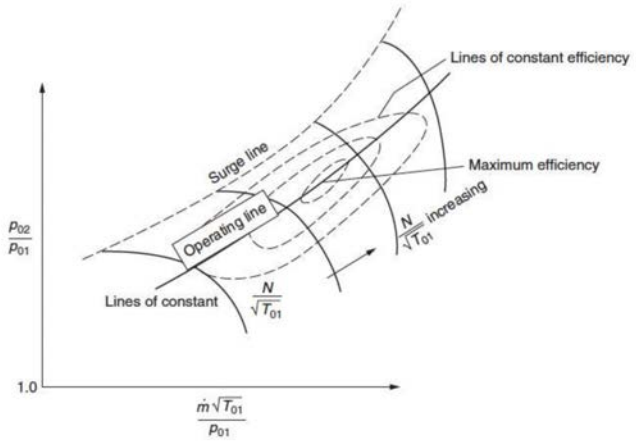

Figure 6: Compressor map [6]

the first line of such importance is the surge line, above which the compressor stalls. As a matter of fact, it is considered as the compressor stability limit; if an operating point is beyond that line the machine starts to unstably behave and all the performance drastically fall. The curves that present a vertical asymptote are iso-velocity line. This asymptote is the choke limit, which means that it is phisically impossible to reach a higher mass flow rate with that speed line. Moreover, there is also the operating line that relates the behaviour of the compressor when it is connected to the turbine and it indicates in which position the machine is working. Lastly, there are the iso-efficiency lines; the designer, for instance, has the duty to reduce the distance, as much as possible, from the operating line and the highest efficiency line. It must be said that all the properties shown in the figure are dimensionless. They are the result of the theory of the dimensional analysis. As a matter of fact the mass flow along the axis is said to be corrected $\dot{m_{corr}}$ by the parameters T_{01} and P_{01}. For instance they represents the total temperature and pressure respectively at the inlet of the compressor; in this way it is taken into account any small variation on the condition.
Fig. 7 shows how the compressor map is affected by multiple factors which cause the reduction of the surge line. The most interesting aspect is the one concerned with inlet distortion, because, as it will be lately discussed, an inner property of an S-duct is the distortion of pressure. The loss in terms of PR along with the inlet distortion can be quantified as following:

$$\Delta PRS = |(R_{clean} - R_{distorted})/R_{clean}| \tag{5}$$

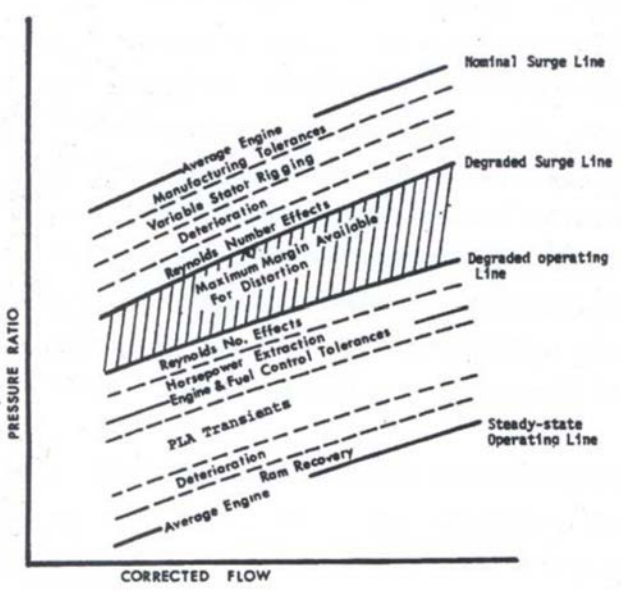

Figure 7: Destabilizing factor of a compressor [11]

where R is the PR at surge, as illustrated in Fig. 8. But since the quantification of the distortion is not in the purpose of the thesis, it is just important to understand how the surge, and therefore, the stability of the compressor is affected by it.

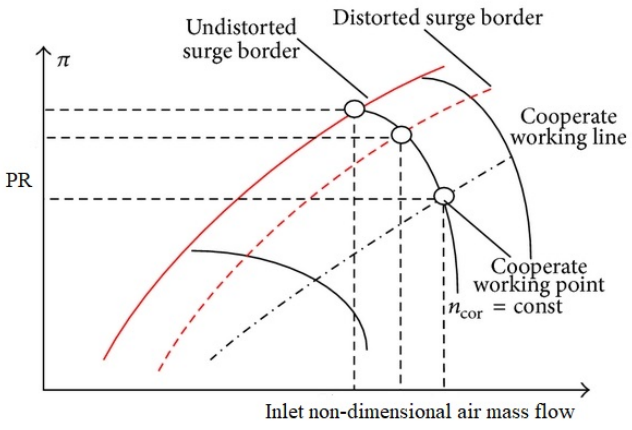

Figure 8: Surge pressure ratio loss

1.2 Transonic Axial Compressor

A transonic axial compressor is defined as a compressor in which the relative mach at the inlet is supersonic ($M > 1$), and, therefore, at the exit it becomes subsonic ($M < 1$). For instance, the transonic compressor is linked with the demand of high thrust of the future turbofan engines, which brings about high rotational speed [22]. Nowadays, the interest in these machines is extremly increased due to the will of reaching high pressure ratio along with a consistent efficiency. A slight increment in the percentage of the efficiency could save lots of fuel cost as well as determine a key factor for product success [8]. Moreover, if the pressure ratio is increased along a single stage, this implies the reduction of dimensions (size and weight) of the engine with a cutoff of the production costs. For this aspect, nevertheless the research of this type of compressors is widely spread, it is meant to further increase. As stated in [5] the PR can easily reach values up to 2 (despite the 1.3 in the subsonic compressor), but, on the other hand the efficiency is fixed around 90%. This drawback occurs becuase of the complexity of the flow field that is created inside the compressor, which is transonic. Hence, the outer span of the blade experiences a supersonic flow fied, whilst the inner span remains subsonic [17]. Furthemore, the presence of a supersonic fluid induces severe shock waves, which consistently affect the efficiency of the machine.

1.2.1 Blade-to-blade Flow Comparison

The supersonic profile, due it experiences supersonic flow cannot be similar as the subsonic one. This one, for instance, if it is invested by a flow with Mach over 0.7-0.75, it is going to accelerate due to its rounded leading edge. As a matter of fact, there is the creation of the sonic bubble (as shown in Fig. 9) in which the flow is at a $M > 1$, and hence the profile is defined as transonic.

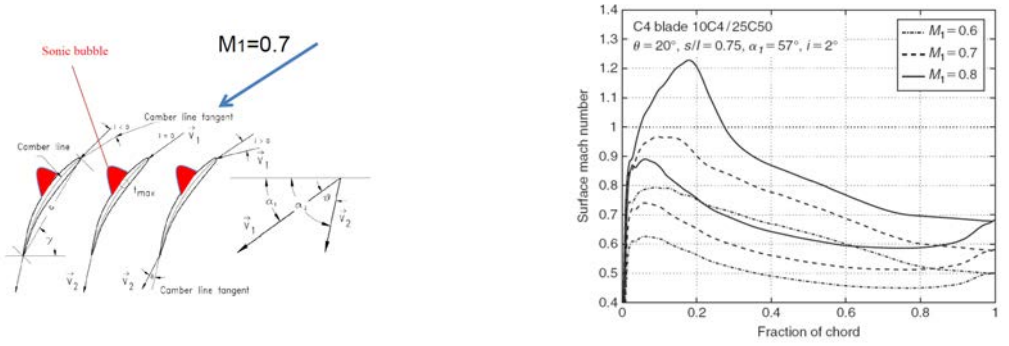

(a) Sonic bubble over a conventional subsonic profile

(b) Variation of surface Mach number with different Mach at inlet

Figure 9: Effect of a high Mach at inlet in subsonic profile [4]

From Fig. 10 it is clearly shown how the supersonic flow behaves while encountering a subsonic profile. There is the creation of the bow shock detached from the profile which causes two different zones; the first one is subsonic in which the shock is almost normal, hence the reduction of the Mach is consistent, while the latter one is far from the leading edge and the shock is too weak and the flow remains supersonic.

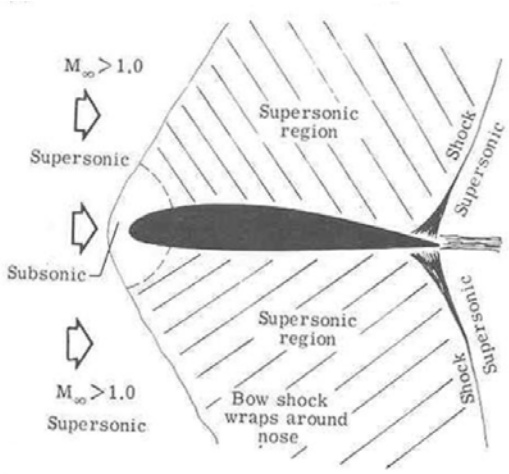

Figure 10: Conventional subsonic profile with a supersonic flow

It is interesting to notice how in the subsonic area the flow accelerates, and almost the entire suction side is governed by a supersonic flow field.
In order to create an attached oblique shock, which is the aim of the supersonic balde, the LE should be spiky. Indeed, the shape is way different from the conventional ones (see Fig. 11). As a matter of fact the ratio between maximum thickness and chord ($\frac{s_{max}}{l}$) is around a value of 0.04, which highlights how narrow the profile is.

(a) Supersonic profile (b) Subsonic profile

Figure 11: Comparison between conventional subsonic profile and supersonic profile

The differences are easily visible; in fact, the 11a is highly sharper than 11b to prevent the bow shock with the maximum thickness over the 50% of the chord length.

1.3 Shock wave theory

Shock waves are irreversible processes, which occur in extremely thin regions [3]; the consequence is the generation of entropy entailing a drastic in the properties of the flow. As a matter of fact temperature, pressure and density instantaneously increase, by maintaing the total temperature and enthalpy costant (at least in the normal shock). This happens due to the fact that either the shock wave is a no-work process or there is no heat addition. This phenomenon might happen into three different ways:

- Normal shock wave
- Oblique shock wave
- Bow shock

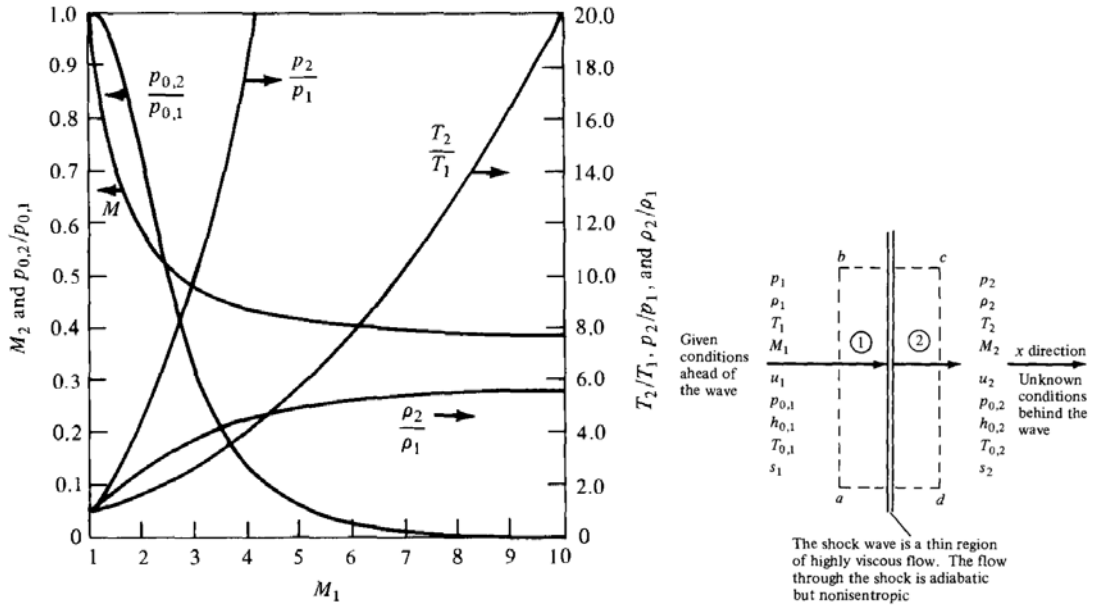

(a) The variation of properties across a normal shock wave as a function of upstream Mach number: $\gamma = 1.4$ [3]

(b) Sketch of a normal wave [3]

Figure 12: Normal Shock wave configuration and properties variation

The normal shock wave is so-called because the postion of the wave is perpendicular to the direction of the flow, like it is represented in the Fig. 12b and, as stated before, the properties rapidily vary; specificaly, the supersonic condition upstream of the shock is instantaneously turned into a subsonic condition downstream. Moreover, by taking into consideration the equation 6, the Mach downstream (M_2) depends only by the Mach upfront of the shock. For instance, the more the Mach increases ahead of the

wave, the more it decreases after the shock; as a matter of fact the limit is set to 0.378 when $M \longrightarrow \infty$.

$$M_2^2 = \frac{1 + [(\gamma - 1)/2]M_1^2}{\gamma M_1^2 - (\gamma - 1)/2} \tag{6}$$

However since the calculation across the shock are not object of the study, it should only be said that all the relationship between the properties are tabulated in tables with the parametric value of γ.

As it is concerned with the oblique shocks, these are occuring when the angle between the flow and the wave is not 90°, but, as stated in [3] "the shock wave will make an oblique angle with respect to the upstream flow". What is interesting to highlight is that when a supersonic flow encounters a corner it might have two different behaviours, with respect to the angle of it. In fact, the distinction between oblique shock and expansion waves might be done. If the angle of the sharp body is concave the flow experiences an oblique shock with a continuous rise of the pressure, otherwise, if the angle is convex the flow is accelerated and the pressure continuously decreases as can be seen in the following figure.

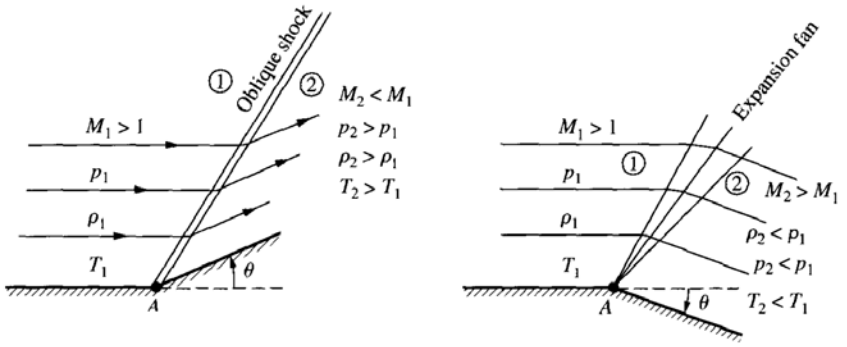

Figure 13: Supersonic flow over a corner [3]

Furthemore, it is possible to see how the flow is deflected by an angle θ from is axial direction, and, therefore the velocity can be split into the tangential and normal components. From the equation of continuity along the tagential direction, it is possible to work out the fact that the tangential component of the velocity remains constat across an oblique shock ($w_1 = w_2$) [3]. Even for this phenomenon all the relations of the properties are tabulated and, it might be found an equation for the Mach number downstream of the shock wave similar to the eq. 6.

$$M_2^2 = \frac{M_{n,2}}{sin(\beta - \theta)} \tag{7}$$

Eq. 7 and 6 are resembling each other; in fact they both state the dependency of the

Mach number behind the shock. In this case of an oblique shock, the Mach downstream is governed only by both the normal component of the upstream Mach and the two angle β (wave angle) and θ (deflection angle).
Finally, the last step to conclude the study of the oblique shocks is the $\theta - \beta - M$ relation. As a matter of fact, from the continuity equation and recalling the constancy of the tangential components, the relation is given by equation 8.

$$tan\theta = 2cot\beta \frac{M_1^2 sin\beta - 1}{M_1^2(\gamma + cos2\beta) + 2} \tag{8}$$

The previous equation returns the values of the deflection angle as a function only of M_1 and β and it can be plotted as in Fig. 14a. Two areas are found in the $\theta - \beta - M$ diagram because once θ and Mach are set, there are two possibilities of β. This fact is related with the idea of strong and weak shock (see Fig. 14b); above the red line the flow field becomes subsonic (strong shock), whilst below that line the flow remains supersonic (weak shock). Actually, there is a second line (blue one) that is called sonic line which divide the zone in which $M < 1$ and $M > 1$. However, between the two lines there is a narrow area, in which even if the weak shock occurs, sometimes it can barely happen that the downstream Mach is subsonic. The red line connects all the maximum

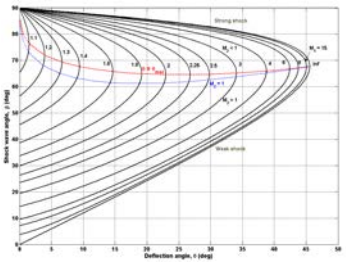

(a) $\theta - \beta - M$ relation

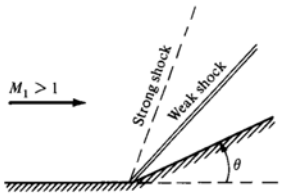

(b) Weak and strong shock waves [3]

Figure 14: Oblique shock waves properties and configurations

deflection angle of each iso-Mach line; in fact for every Mach number a maximum value of θ (θ_{max}) is set. Moreover, the nature implies that there is no solution when $\theta > \theta_{max}$: in particular no attached oblique shock is established, but, the new phenomenon that is created is a bow shock (detached from the blunt body).

The distance between the wave and the body is δ and it is called shock detachment distance. It is interesting to understand how the shock is developing along the wave. The point a, for instance, is the point in which the shock wave is normal and it represents the strongest decelaration of the flow. Once the flow encounters the wave away from point a, the shock becomes weaker and curved, and sometimes it reaches the condition of the Mach wave. In addition, in the point b the shock is oblique and it

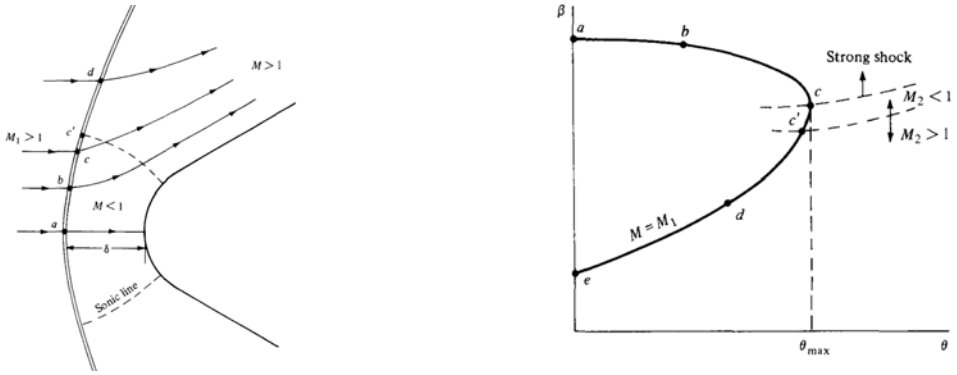

(a) Flow over a supersonic blunt body [3] (b) $\theta - \beta - M$ diagram for a bow shock

Figure 15: Bow shock configuration and $\theta - \beta - M$ diagram

is a strong wave as it is shown in Fig. 15b, therefore the Mach becomes subsonic; the point c is the point of maximum deflection angle above which (from c to d) the Mach pertains in its supersonic flow field. Finally the parameters of the shock (δ, shape and flow field) are only function of the upstream Mach number and the shape of the body.

1.3.1 Shock waves in a compressor cascade

As briefly discussed in the previous section, a supersonic flow brings about a shock wave, which has a 3D structure; in addition the birth of this shock is the main cause of the rise of the pressure along the compressor. Moreover, when shock waves occur, the blase experiences two different flows; the outer part is overwhelmed by a supersonic flow, while the inner part is subsonic. This happens because of the particular configuration of the waves (see Fig. 16). On the other hand, the drawback is that it penalizes the efficiency of the rotor; plus, if it is combined with the tip clearance flows, it might create problem as it is concerned with the stall. The secondary tip clearance flows will be lately examined, when it will discuss about losses in transonic compressors. As it might be understood, the flow is extremely complex inside a transonic compressor, and the designers should take into consideration all the possible effects that might occur (shock waves, seconday flows, boundary layer/shock interaction [9]).
However, the configuration of the shock waves inside a transonic compressor cascade is the one shown in Fig. 16.
Immediately, an oblique shock appears attached to the LE, that is called bow shock, whilst, inside the channel betweeen two blades, there is the creation of a normal shock wave called passage shock. The last one produces a major rise in the pressure, rather than the bow shock; as explained in the previous section, the normal shock is way stronger than the oblique and the therefore the pressure increases much more. In fact,

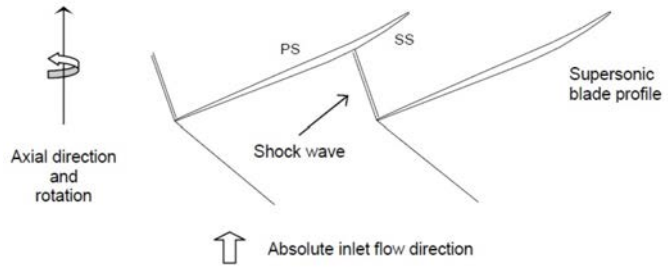

Figure 16: Sketch of shock wave in a supersonic cascade

once the flow encounters the first wave, it still pertains its supersonic condition behind of it, due to a weak shock; but then, when the flow arrives in the middle of the channel it creates a normal shock, downstream of which it is subsonic. Actually, the configuration shown in Fig. 16 depicts a particular condition that is the one of design operating condition. Once the compressor moves along the speed line the configuration changes by varying the position of the shock. As a matter of fact, if the back pressure is increased, this means that the operating point is moving towards the stall limit; in this case the bow shock is detached from the LE (Fig. 18). Contrarywise, if the back pressure is lowered, the condition reached is the choke. In a nutshell, when the operating moves from the choke condition to the surge line, the position of the shock wave is shifted upstream resembling to a normal shock. This happens because the mass flow rate diminishes and, therefore, the incidence of the flow is increased. All of this is summed up in the following figure.

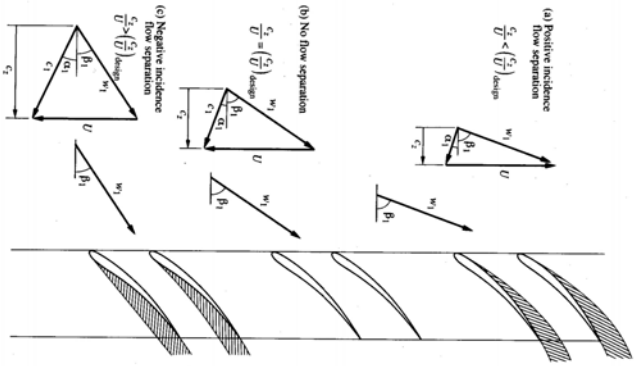

Figure 17: Blade configuration on and off design

Figure 18 highlights that might happen that the shock wave negatively interacts with the SS boundary layer of the blade. This provoke the thickening of the local BL, which brings about the creation of a bubble (Fig. 19) which might reattach before the

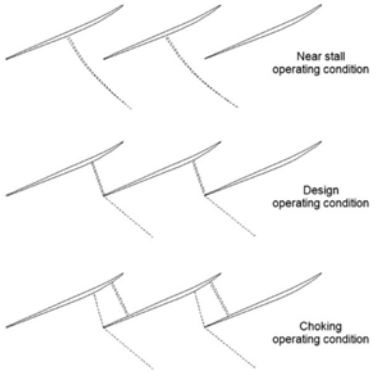

Figure 18: Impact of operating condition on a transonic cascade (constant wheel speed) [9]

TE or not. If not, the aerodynamic losses are consistent and the efficiency is highly damaged [9].

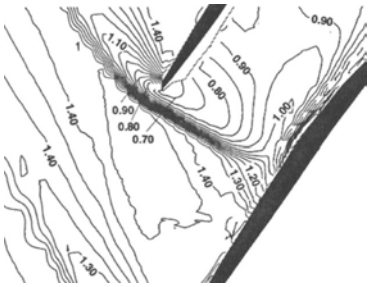

Figure 19: Blade-tp-blade M_{rel} in a transonic compressor [27]

1.4 Losses across a transonic stage

The transonic compressor stage it is a real challenging machine due to the complexity of its inner flow field. As a consequence of that, the estimation of loss in supersonic compressor blades has been a subject of major concern [17]. The losses, indeed, are not comparable with the one of a subsonic cascade; in this case are considered of primarly importance.
In a rotor the main sources of losses have been identified in:

- Endwall mixing flows
- Hub corner losses
- Shock losses

One source of loss is surely the endwall region, where there is a thin gap between the casing and the rotating blade, in which secondary flows occur. Due to the reverse gradient of pressure between SS and PS, the fluid is driven into the gap and it is spread inside the passage as depicted in Fig. 20. When this secondary flow interacts with the

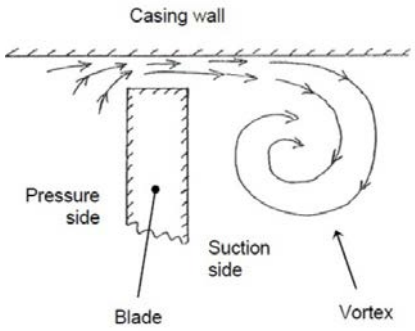

Figure 20: Tip leakage gap secondary flow [7]

main flow it creates the so-called tip clearance vortex or tip leakage vortex, which starts at the leading edge and develops into the passage [7]. These endwall flows plus the interactions with the BL in the casing wall entails blockage and instability on the flow properties which bring about aeerodynamic losses.
As it is concerned with the hub corner losses, this phenomenon is shown in Fig. 21. This loss is positioned near the SS of the blade hub and it is related with a viscous effect of the BL, by which the flow migrates towards the tip wall [21]. In addition, as it was discovered by [1], the nearer the compressor is at the surge line (stability), the more the hub losses increases; this can be notice in the Fig. 21.

Furhtermore, as already stated, a shock wave has a severe impact on the overall performance of the compressor. In fact, taking into consideration Fig. 19, the interaction

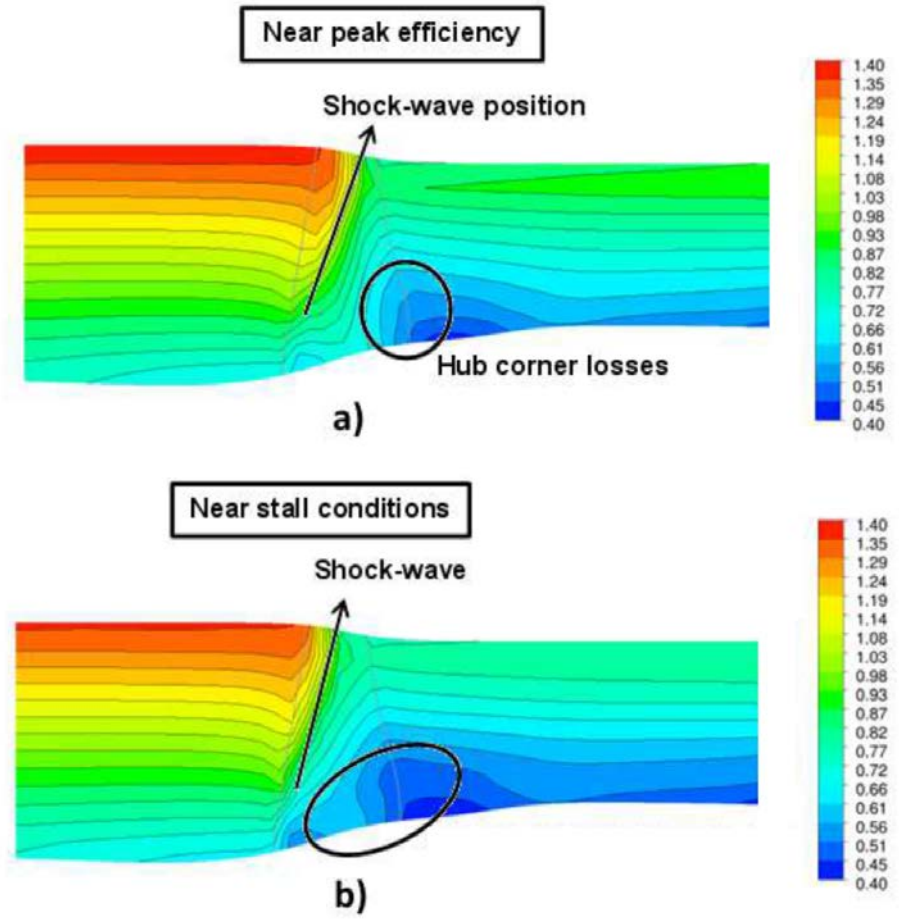

Figure 21: M_{rel} contours in meridional view of R67 baseline. a: Near Peak Efficiency b: Near Stall Condition [21]

between the passage shock and the BL of the SS creates the a sort of bubble in which the flow is reversed. That bubble might or not reattach by the end of the TE, but is so does not happen the wake is propagate. The more the wake is propagated, the more the aerodynamic losses increases. Many studies have been done about the prediction of these losses, but, due to the unpredictability of the flow this is highly tough. By now, the most accurate method of calculation is the Navier-Stokes for three-dimensional flow.

1.5 NASA Rotor 67

The Rotor 67 (R67) is a transonic low aspect-ration fan developed by NASA and it represents the first stage rotor of a two stage fan. The properties of the R67 are reported in Table 1 and they are referred to the design operative point. Lots of studies has been conducted on this test case, but the most of them are related with the blades's

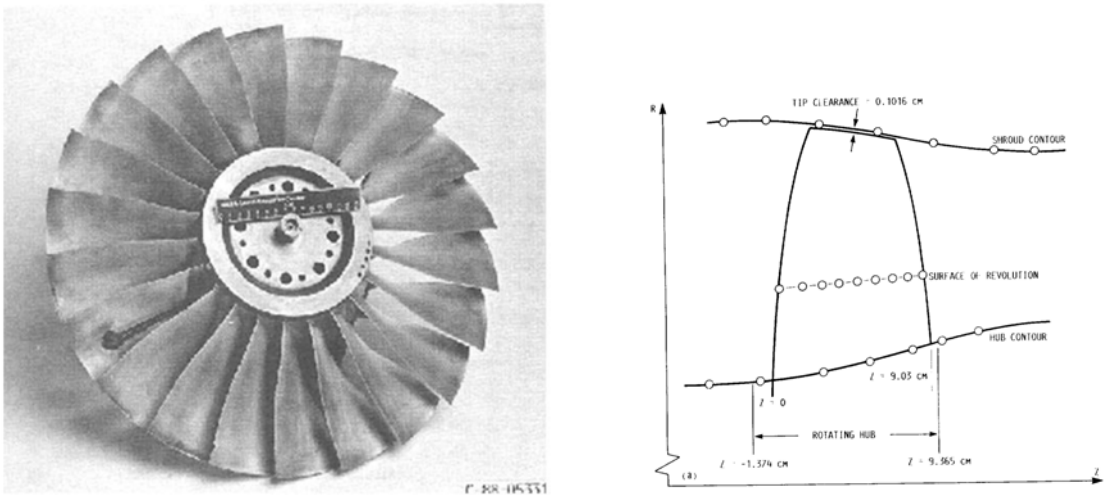

(a) Geometry of the R67 (b) Meridional projection of the blade

Figure 22: Features of the NASA Rotor 67 [26]

optimization. Despite of that, they were of such huge importance along the validtion studies to obtain a high fidelity model with which it was possible to do further researches.

Table 1: Properties of R67

Properties	Value
Compression Ratio (PR)	1.63
Mass Flow Rate	33.25 $[\frac{kg}{s}]$
Rotational Velocity	16043 $[rpm]$
Tip Velocity	429 $[\frac{m}{s}]$
M_{rel} at inlet	1.38
Number of Blades	22
Inlet Diameter	51.4 $[cm]$
Outlet Diameter	48.5 $[cm]$
Shroud Tip	0.1016 $[cm]$

Chapter 2

S-duct intake physical aspect

S-ducts intake is a non typical intake that might be found both in civil and military implementation. Nowdays, the research to employ offently this intake is trying to develop cutting-edge solutions and configurations. In addition, because of its shape, the curvature creates a singular inner flow which should be accurately investigated and characterized. Moreover, the main insterests in those components is their potential contribution in noise and drag reduction [13]. Therefore, the main purpose is on figuring out how to design it and how to reduce the fuel comsumption.

2.1 BLI (Boundary Layer Ingestion)

Nowadays civil aircraft are designed in a way in which the engine is place far from the fuselage in order to avoid the ingestion of the slow flow that is developed on the aircraft's surface. The future concept of aircraft is the BWB (Blended Wing Body) due to its possibility to allow the placement of the engine near the TE and, consequently, they pick up "large amounts of aircraft boundary layer which makes BWB aircraft more than suitable for a BLI propulsion system " [20]. In this way the slower flowing of air is ingested by the engine (place on the rear) and exploited to create the needed thrust.

Figure 23: Example of a Blended Wing Body (BWB)

In addition, the main difference between the traditional aircraft and a BLI aircraft

is concerned with the inlet distortion; the airflow, indeed, is no more clean, but it is said to be distorted due to the presence of the aircraft itself. In fact, the interaction between the engine and the fuselage is closer than in the conventional ones, because the inlet condition of the fan is function of the shape of the aircraft. This is reflected even in the reduction of the drag, because they are a sort of unique body and, hence, part of the drag of the aircraft is driven into the engine. As a consequence of that, the airplane needs less thrust to fly at the same speed, due to that reduction in the drag, and the consumption of fuel is lowered. The following figure shows the two different configurations and how a BLI aircraft is aerodinamically improved. Moreover, without deepening in the calculation since it is not in the interest of the work, the loss of kinetic energy is utterly decreased at the downstream of the fuselage.

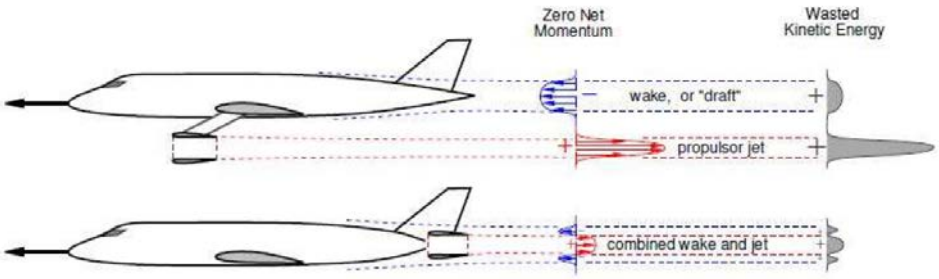

Figure 24: BLI and conventional aircraft comparison

The real challenging problem is to design cutting-edge fan in order to bear a high distorted flow, without losing lots of efficiency. As it is possible to analyze from Fig. 25, the fan should create the expected PR by preserving a high efficiency, with a non-clean flow. What the swirl is and how the pressure distribution affects the fan's overall performance are lately discussed.

2.2 Swirl

El-Sayed et al. in [15] adfirm how the swirl phenomenon might cause severe problems in the aircraft engine, such as vibration and surge. This property is peculiar of an intake with a curvate (e.g. S-duct intake) and it is useful to outline the rotation of the inner flow. It is commonly measured at the AIP (Aerodynamic Interface Plane) to avoid any perturbation from outlet and, it estimates how the flow is deviated from the axial direction. Hence, the angle that is created is:

$$\alpha = atan(\frac{U_\theta}{U_Z}) \tag{9}$$

where U_Z is the axial velocity and U_θ is the tangential velocity.

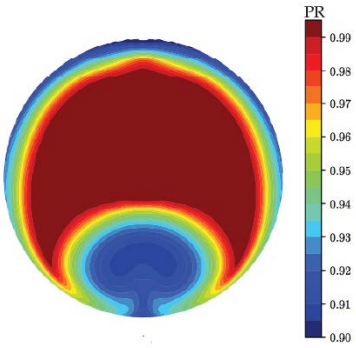

(a) Pressure distribution at the AIP of an S-duct

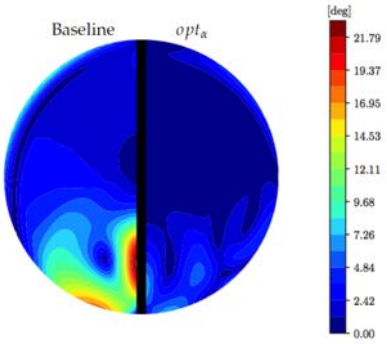

(b) Comparison of swirl distribution at the AIP of an S-duct and and optimized geometry

Figure 25: Pressure and Swirl configuration at the AIP of an S-duct

From Fig. 26 it is understood that the swirl is said to be positive when it has the same direction of the rotation of the compressor, whilst negative when it is opposite. The swirl is a detrimental effect and has three different ways in which it might develop:

- Bulk Swirl
- Paired swirl
- Cross-flow swirl
- Tightly-wound swirl

2.2.1 Bulk Swirl

The bulk wirl is depicted by a single direction of rotation of the flow (see Fig. 27). The sense of rotation can be either the same of the compressor or opposite to it; in the former case it is defined as co-rotating bulk swirl, while the latter is the case of a

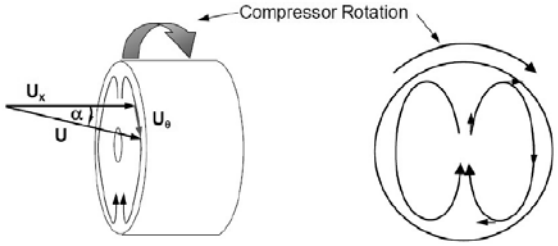

Figure 26: Definition and schematic illustration [10]

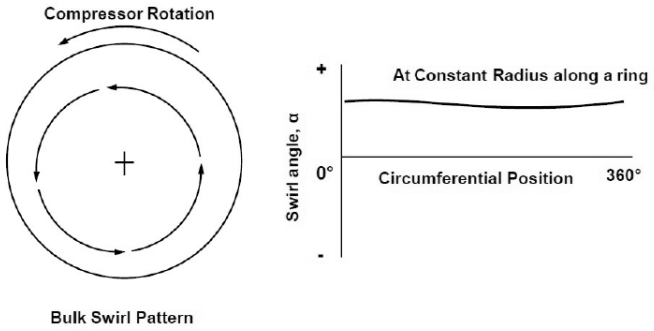

Figure 27: Bulk Swirl representation

counter-rotating bulk swirl.
This phenomenon is the consequence of a non-symmetrical pressure distribution which forces the fluid to rotate in a single direction. The way in which it is developed is different; the co-rotating occurs when a vortex in insgested into the engine, on the other hand, the counter-rotating is internally generated.

2.2.2 Paired Swirl

This type of swirl consitsts in the creation of two vortexes inside the duct with the same or different magnitude; the first is called twin swirl, while the second is the offset paired swirl. To easily visualize its development is shown in Fig. 28 and it helps to understand it.
At the beginning of the duct, the flow is not disturbed and the trend of the pressure is clear, but as long as the flow approaches the curvature the fluid starts to whirl. Moreover. the static pressure rises with a reduction of a velocity flow and the BL start to create. The flow is governed by a non-uniform momentum distribution because the flow field is not homogeneous; the velocities vary from a zero value at the wall to a maximum value in the center of the intake. Due to the high momentum of the center flowfield, this is dragged towards the upper wall and with the low-momentum fluid the opposite happens (it slides along the lower part). The concomitance of this two effects

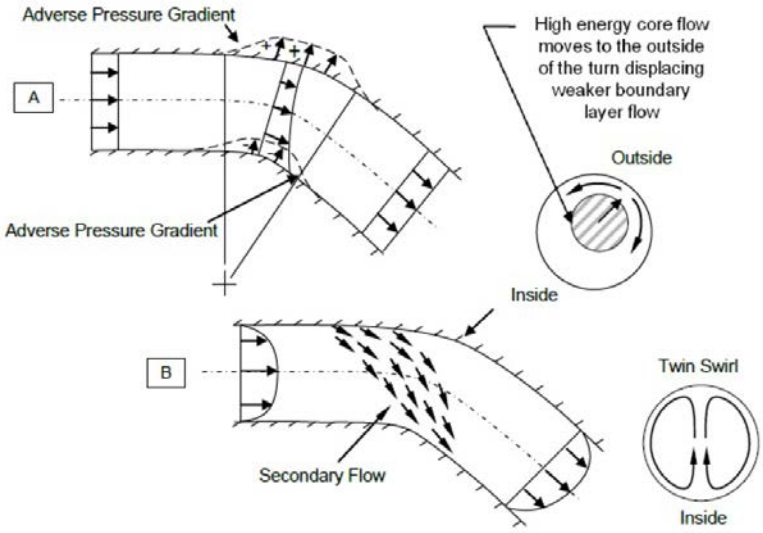

Figure 28: Paired Swirl representation

brings about the two paired vorteses.

2.2.3 Cross-Flow Swirl

Likewise the previous one, two vortexes are created but with the only execption that the momentum ditribution is homogeneous due to a uniform velocity.

2.2.4 Tightly-Wound Swirl

This swirl gives birth to a vortex attached to the ground or to the airplane fuselage (see Fig.29) and they are consequences of LE extensions, tip vortex or ground operation.

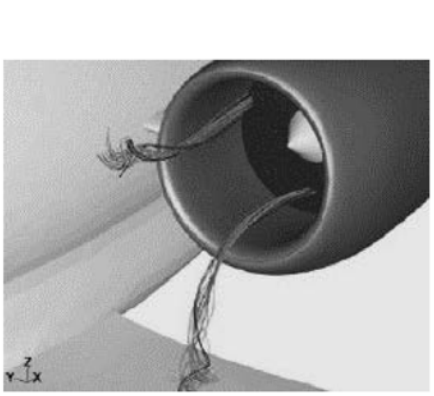

(a) Tightly-wound vortex attached to airplain surface [10]

(b) Tightly-wound vortex attached to the ground [10]

Figure 29: Example of tightly-wound swirl

In this work the most relevant swirl is the paired one, because it is going to be as inlet condition for the fan downstream of the S-duct by affectting the overall performance.

Chapter 3

NASA R67 Computational Analysis

In this chapter, the computational analisys is carried out from the validation of the model to the matching of the fan and an S-duct intake. Initially the model was studied by introducing several types of meshes, therefore a light mesh indipendency analisys was carried out. The initial part of the research is concerned with the understanding of which mesh was able to reliably describe the flowin the single channel with uniform initial condition. Once this step was overcome, the attention was moved on the representation of the full anulus and, to perform that, it was necessary to study the geometry of the ogive upstream of the fan. Finally, there is the matching of the two machines (fan and S-duct); this was a huge time-demanding step to perfectly set the parameters of the simulation.

The software used for all of the simulations are:

- CFX-TurboGrid for the generation of the mesh of the rotor
- CFX-Pre-Solver to set the parameters for the simulation
- CFD-Post to visualize the results and to the post-processing
- Fluent to analyze the behaviour of the S-duct
- SolidWorks to create the geometry of the ogive
- ANSYS Workbench to create the mesh of the ogive

All of these calcuation are done by exploiting the Delta cluster of Cranfield University, which was highly useful to reduce the computational costs.

3.1 Computational set-up of the model

The first step to start a computational analisys is to validate the model, which means comparing the computational results to the experimental ones. For instance, if the deviation of the results is too remarkable fron the real ones, the model could not be use for further researches because it is not representing the reality. The problem is that the deviation could be entailed by multiple causes and the challenging aspect relates on understanding where to better investigate. As a matter of fact, the simulation highly depends on the initial parameters such as which model and order are used to solve

the Navier-Stokes equations, which turbolence models is more appropriate to faithfully describe the BL or the wake of the profile, the number of iterations and the value of the residuals. Said that, this step is a time consuming step which might required several weeks to outline the right configuration.

The geometry of the rotor is not a CAD model, but the coordinates of hub, shroud and profile (provided by NASA in [26]) were properly formatted to act as input file for the the creation of the model in ANSYS CFX-TurboGrid. The result of the re-construction of the blade is shown in Fig. 30.

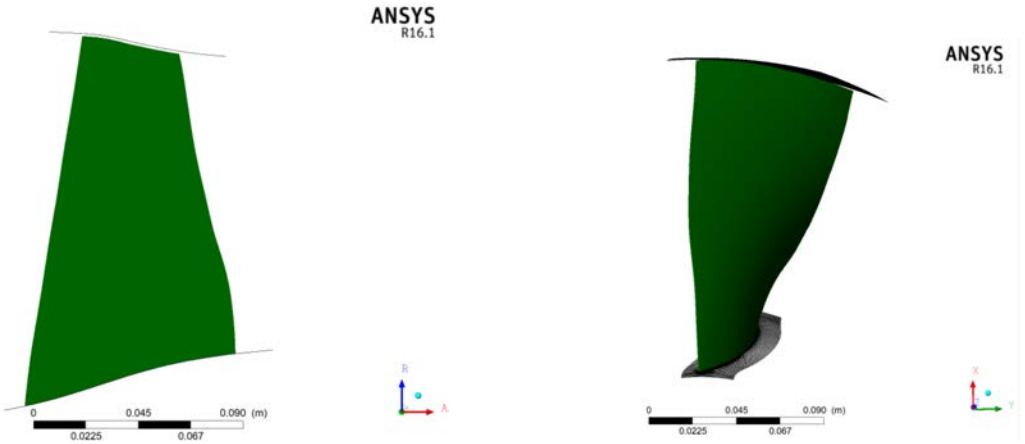

(a) Meridional veiew (b) Frontal view

Figure 30: Meridional and frontal views of the blade re-constructed in ANSYS CFX-TurboGrid

3.1.1 Computational Grid Generation

The comptational grid has been developed in ANSYS CFX-Turbogrid environment, which perfectly suits for the studies of the blades. A blade domain is based on three different parts (see Fig. 31):

- inlet, that should keep the fluid in his initial state
- outlet, that should capture what happens near the TE and the effect of the wake
- passage, that contains the blade itself

The last one is the most critical because the simulation is highly dependant on the mesh's quality; the phenomenons, for instance, that occur inside a transonic fan are really complex and need to be analyzed with accuracy. Once the geometry is loaded and the tip gap is set, the Automatic Topology and Meshing tool (ATM optimized) is used to generate the topology of hub and shroud as depicted in Fig. 32. in order to

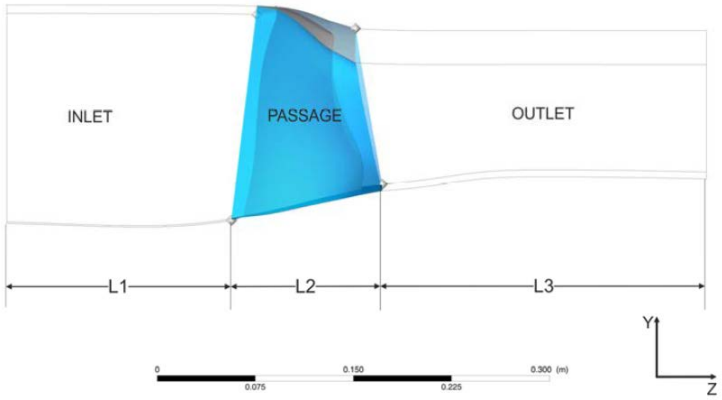

Figure 31: Inlet, passage and outlet configuration [18]

construct the 3D grid, an interpolation of the mesh between hub and shroud is done, but, the problem is that this step could deteriorate the grid. This might be avoid by introducing a number of intermediate layer, which has the duty to better guide the mesh through the spanwise.

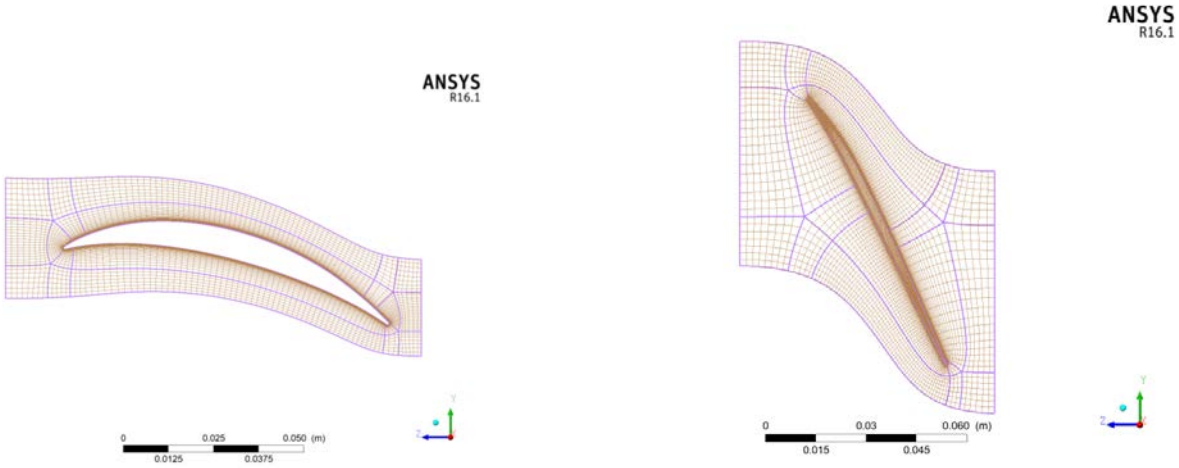

(a) Hub ATM optimized topology (b) Shroud ATM optimized topology

Figure 32: Hub and Shroud configuration

In order to achieve a such accurate grid the number of elements inside the passage is set at 1.5 million, in the gap region 40 nodes are added to better simulate the tip vortex region. However, the utterly sensitive part is the boundary layer because the precision of the calculation are function of the value of y^+. This property is linked with the height of the first cell near the blade, and its value depends on the turbulence model that is implemented. Actually, having said that, the smallest the y^+ is, the more accurate the simulation is, but, despite this fact, the computational cost incredibly and rapidly boosts. Hence, it is necessary to find a trade-off between these two aspects.

In this case, the value of the height of the cells (y^+) is, approximately, set around 0.1. The final mesh shown in Fig. 33 (mesh's passage) implies 2 millions of nodes.

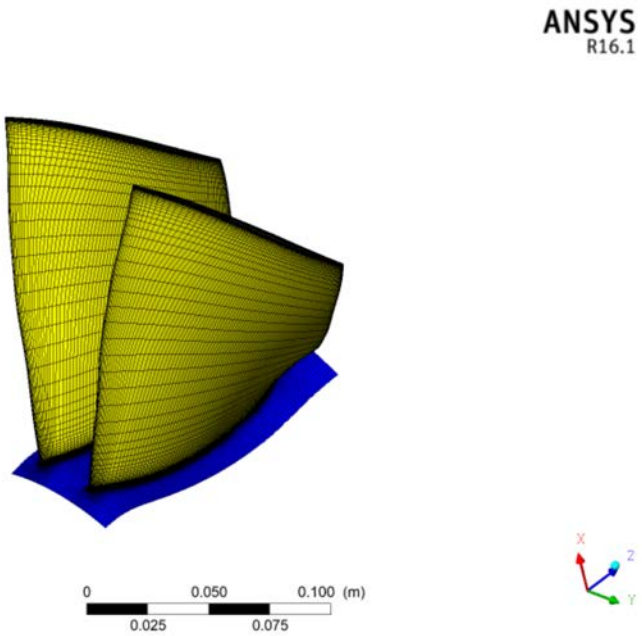

Figure 33: Mesh of the passage

3.1.2 Turbulence modeling

Engineering problems are offently related with turbulent flows. The unpredictability of this flowfield implies an accurate selection of the turbulence model and near-wall approach to simulate the phenomenon. Once the flow is said to be turbulent, in CFD application the approaches that might be used during the calculation are three:

- DNS, Direct Numerical Simulation
- LES, Large Eddy Simulation
- RANS, Reynolds Averaged Navier-Stokes Simulation

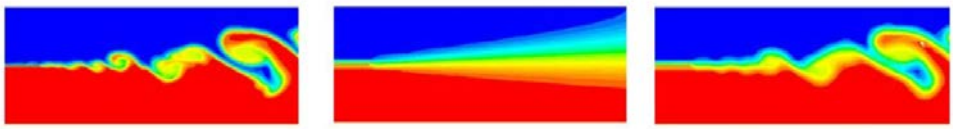

Figure 34: DNS, RANS and LES examples

Since it is not in the interest of the work to fully understand and study the turbulence approach, it can be said that the most accurate are the DNS, because it resolves the

full unsteady N-S equations. Despite of that, the computational cost is prohibitive. LES models are less time-consuming, but this is still too much for most of the practical applications. Therefore, the turbulence model used is the RANS one, that although it is not that highly trusty, the cost of the simulation is much lower than the others. Once the computational approach is set, it is necessary to understand which turbulence model might be implemented during the calcultation. For this research the SST $k-\omega$ model is used, due to its more accuracy in predicting the behaviour of the flow rather than any other RANS models. If the problem requires a coarse estimation of turbulence becuase it is more strongly function of other physical asoects, the $k-\epsilon$ should be used. Finally, as it is concerned with the near-wall region the strategies available are two:

- Wall Function, which saves computational costs using empirical equations. As stated in [19] this choice is suitable for problems where the attention is focused in the middle of the domain rather than in the BL. Consequently, the restriction on y^+ is not that strict; indeed, it can reach values between 30 and 300.
- Low-Reynolds-Number, where y^+ requirement are very tight ($y^+ \approx 1$). Therefore, a very fine mesh is needed near the wall bringing about a large number of nodes. This models perfectly suits for turbomachinery performance because the forces and heat transfer are well described.

3.1.3 CFX-Pre Set-up

CFX-Pre is an ANSYS's tool with which all the parameters of the simulation are set. In the next table all of the relevant parameters are reported.

Table 2: Set-up of the parameters in CFX-Pre

	Ansys CFX Solver set-up	
Analysis Type	Steady State	
Domain	Domain Type	Fluid Domain
	Fluid and Particles Definition	Air Ideal Gas
	Reference Pressure	0 [atm]
	Domain Motion Option	Rotating
	Domain Motion Angular Velocity	-16043 [$revmin^{-}1$]
	Heat Transfer	Total Energy
	Turbulence Option	SST
	Wall Function	Automatic
	Wall Heat Transfer Model	High Speed
Boundary Condition	Hub	No Slip Wall Smooth Wall Adiabatic Rotating Frame
	Shroud	No Slip Wall C-R Wall Smooth Wall Adiabatic Rotating Frame
	Inlet	Subsonic Stat. Frame P_0 101325 [Pa] Normal to BC Stat. Frame T_0 288.2 [K] Frame Stationary
	Outlet	Subsonic MFR or Pressure Variable
Solver Control	Advection Scheme	High Resolution
	Turbulence Numerics	High Resolution
	No. Iteration	3200
	Timescale Control	Auto Timescale
	Convergence Criteria	MAX 1e-5

Due to the fact that the convergence of the simulation is critical, it was necessary to adapt the maximum timescale between each iteration. Therefore, at the beginning it was set at 1e-7, then was slightly lowered every 50 iteration and in the end increased to 1e-5. This was necessary to guarantee a stable simulation.

3.2 Validation

This chapter deals with the validation of the model for further implementation. The experimental data require to be matched with the less error possible by the CFD simulations. In order to do that, many models have been developed in which the number of mesh elements varies and to understand if it is possible to achieve outstanding results even with a coarser mesh; this, for instance, might save lots of computational cost.

Table 3: Comparison of different type of mesh implemented

	Number of Nodes
Coarse $k-\epsilon$	700k nodes
Coarse	900k nodes
Fine	1.8 mln nodes
Very Fine	2.0 mln nodes

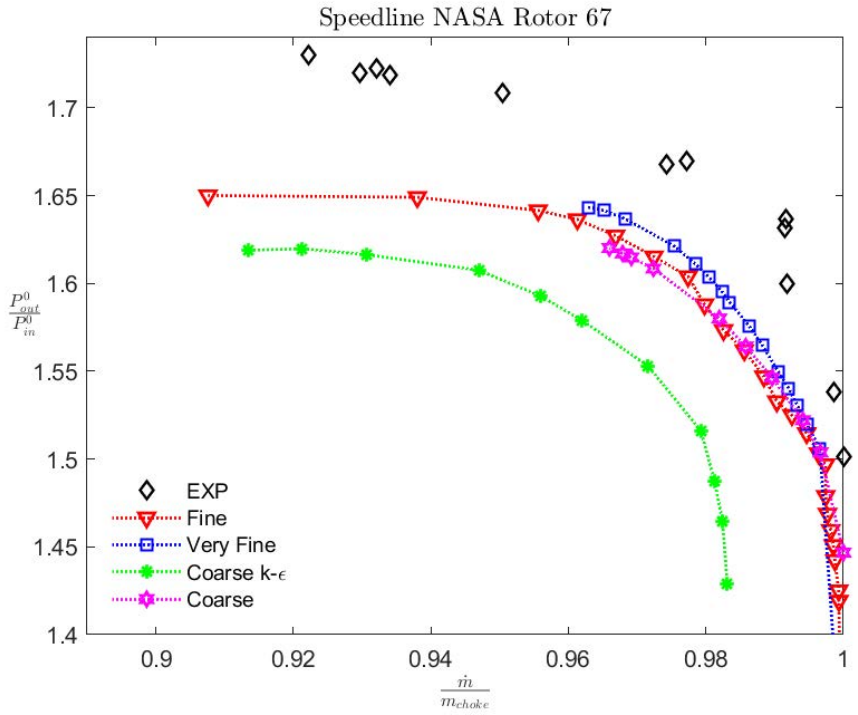

Figure 35: Speed line NASA Rotor 67

The previous figure depicts the speed line of the NASA Rotor 67 when it is simulated with a rotational speed of 100%. The line is obtained by varying the pressure at the outlet, starting from the choking condition and increasing the pressure untill the stall margin is reached. The PR is here reported with respect to the non-dimensional mass flow rate $\frac{\dot{m}}{\dot{m}_{choke}}$. Analyzing the Fig. 35 the trend of the experimental data is almost matched for every model implemented but the error commited during the simulation

varies from mesh to mesh (see Table 4). Furthermore, as depicted in [18] the deviation from the experimental results might still be noticed; moreover, the high fine match, as expected, presents the closest values to the experimental ones. The startling aspect is how the coarse mesh with $k-\omega$ SST model (magenta star in Fig. 35) has achieved very good results. At the end, a simulation with a coarse mesh and with $k-\epsilon$ turbulence model was set to work out how the model would have predicted the phenomenon; but, for instance, the results obtained are the worst of all the simulations done.

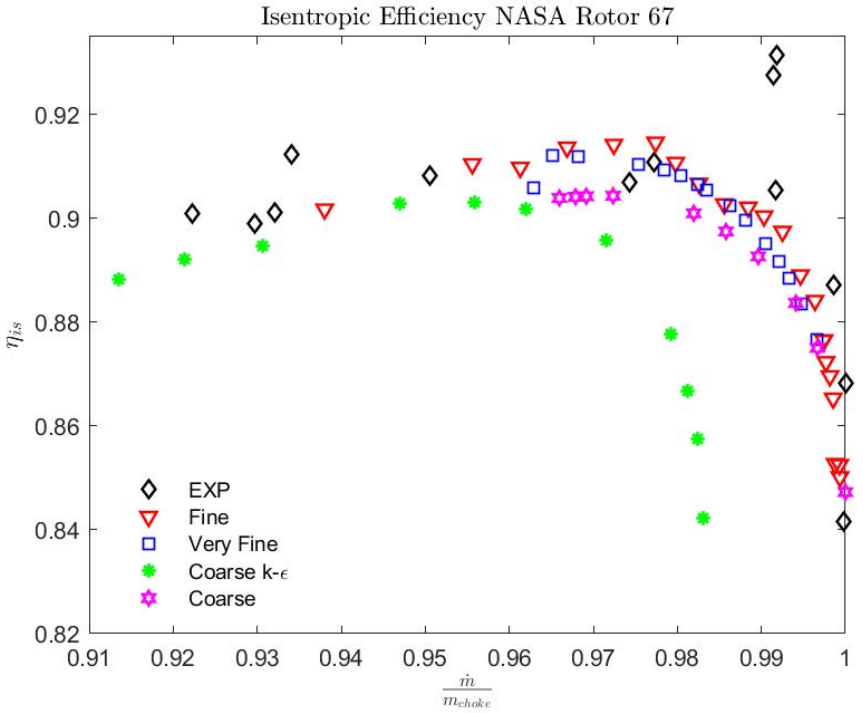

Figure 36: Isentropic efficiency NASA Rotor 67

Table 4: Comparison of different type of mesh implemented

	Mass Flow Rate $[\frac{kg}{s}]$	Relative Error	PR	Relative Error
Design Point	33.25	-	1.63	-
Coarse $k-\epsilon$	33.4185	0.0051%	1.5929	0.022%
Coarse	33.2862	1.08e-3 %	1.6171	0.008 %
Fine	33.4047	0.0046 %	1.6272	0.0017 %
Very Fine	33.2366	4.03e-4%	1.6434	0.0082%

The Table 4 shows the relative error committed by during the simulation. Since the coarse mesh with SSt model faithfully represents the phenomenon, and, since it is 1 million nodes lighter than the two refine meshes, it would be used for further investigation (e.g. R67 map, full anulus and matching with the S-duct simulation). As a matter of fact, the relative error is not that far from the one commited with

the high refine mesh. Moreover, it might be curious and helpful to analyze the trend of the pressure and the relative Mach along the blade for different span and, to see, if possible, the behaviour of the shock wave. Firstly, from Fig. 37 it is noticed how the position of the shock wave is linked with the fall of the Mach number along the blade. This fact is observed in the decrease of the red curves and the relative peak in the pressure curve at the same postion. The greater the pressure is, the lower the Mach is. Furthermore, the Mach number starts exceeding 1, only after the 50% of the span. This occurs because the velocity ranges from low values at the hub to high values at the shroud, since it is radius dependent. This affects the position of the shock as well; the wave, indeed, tends to move towards the trailing edge as the % of span increases. It can be seen that, after the initial fall at the leading edge in the pressure, due to the shock, the profile is quickly stabilized on the pressure side, whilst in the suction side a peak occurs; this is the consequence of the shock wave on the previous blade.

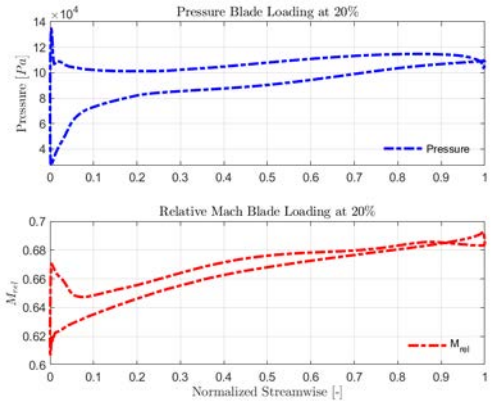

(a) Pressure and Relative Mach Blade Loading at 20%

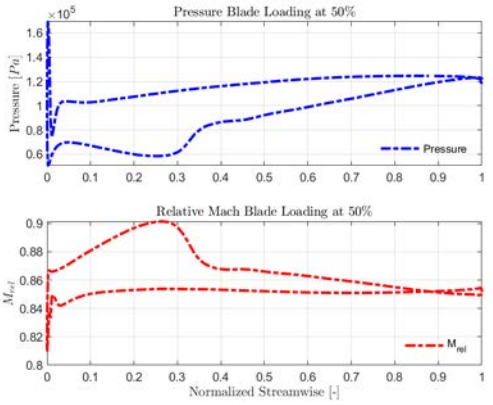

(b) Pressure and Relative Mach Blade Loading at 50%

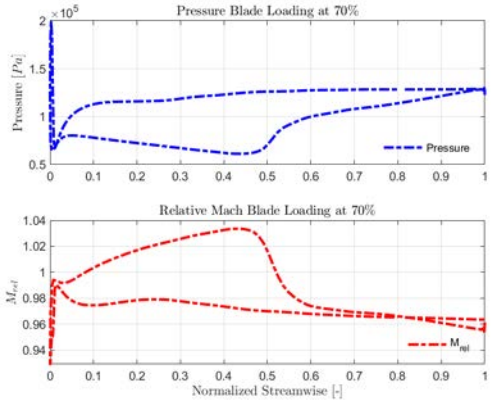

(c) Pressure and Relative Mach Blade Loading at 70%

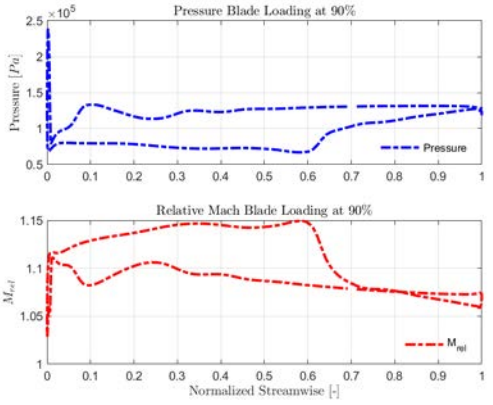

(d) Pressure and Relative Mach Blade Loading at 90%

Figure 37: Pressure and Relative Mach Blade Loading at different span location

From the comparison of the experimental and numerical results (Fig. 38) it can be notice how they are very close each other. As a matter of fact, either the value or the position of the bubble in the suction sidevare almost the same. Even the discontinuity in front of the blade presents the same trend in both of the results.
In addition, the shock wave at the LE is able to reduce the number of Mach the unity, hence, no shock wave occur in the channel. As a matter of fact, as discussed in §1.3.1, this is the situation of the design operating condition, but as soon as this point is abandoned the shock wave is not still enough to reduce the Mach below 1; therefore, a second shock occurs between the blades. The previous situation is the choking condition, in which the mass flow rate is freezed. This is highlighted by comparing Fig. 38a and 39a;in the latter picture the shock near the trailing edge is visible.

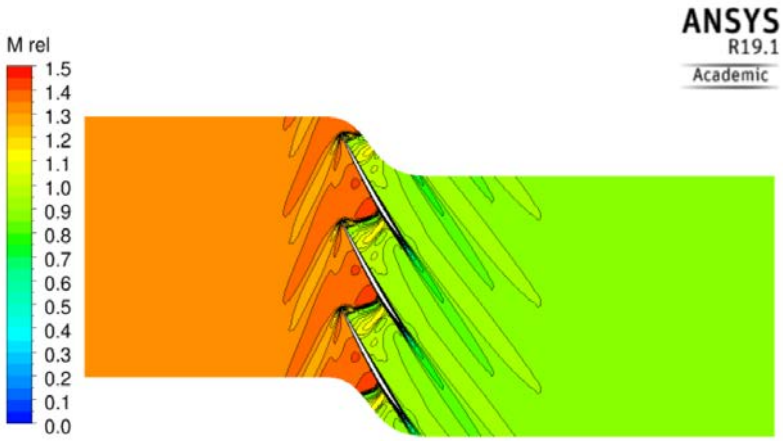

(a) Blade to blade Contour of M_{rel} at 90% near peak

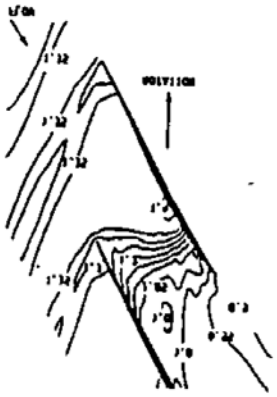

(b) Experimental blade to blade Contour of M_{rel} at 90% near peak

Figure 38: Comparison between contours of M_{rel} of experimental and CFD near peak

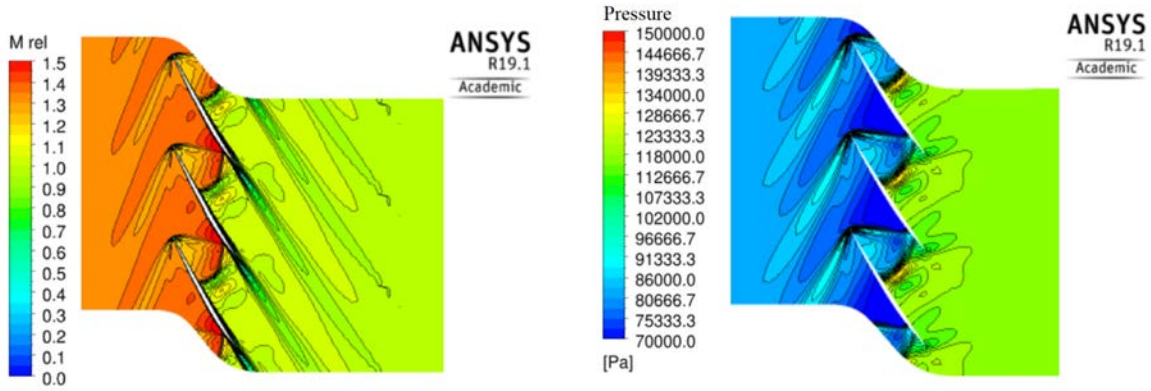

(a) Contours of M_{rel} near choke condition (b) Contours of Pressure near choke condition

Figure 39: Contours of Pressure and M_{rel} near choking condition

3.3 Compressor Map

This section is dealing with the study of the entire map of the rotor R67, in order to have a better idea of the behaviour of th fan at different rotational speed. As a matter of fact, the compressor map is characterized by multiple speed lines, that asymptotically tends to the mass flow at which choking occurs. To do so, the model used was the coarse one; this, for instance, is not far from the results obtained with the finer models and, plus the computational cost is more than halved (4 hours instead of 14). Moreover, to draw all the lines of the map, the rotational speed is changed from 100% to 75% of the design rotational speed. In addition, from surge margin to choking condition the outlet condition set up is the mass flow rate, that varies from simulation to simulation.

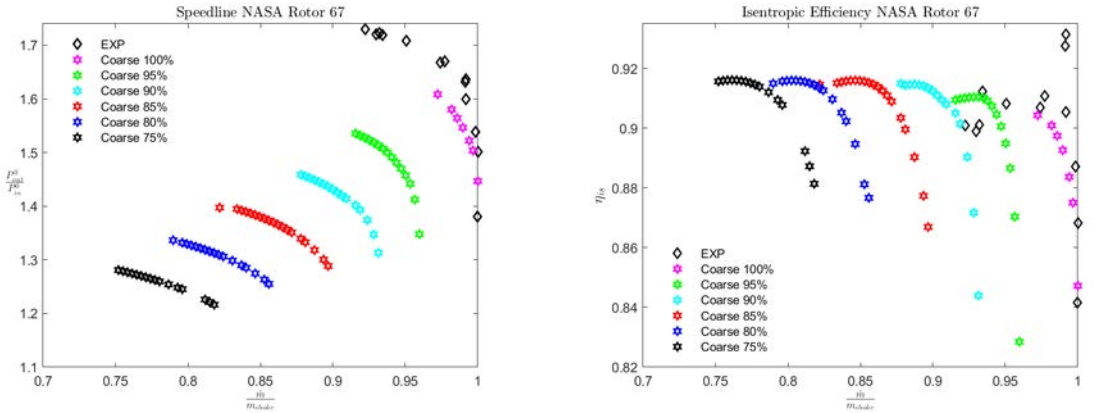

(a) Compressor map NASA rotor R67 (b) Isentropic efficiency NASA rotor R67

Figure 40: Overall performance of the NASA rotor 67

Starting from these data, many conclusions might be drawn. Firstly, the trend of

the compressor is respected; for instance, even if it is not plotted, the stall margin is clear. Moreover, the more the rotational speed is increased, the more the vertical asymptote is abandoned. The next two figures are an example of contours plot of relative Mach at different rotational speed; indeed, the slowest and the 90% cases are evaluated.

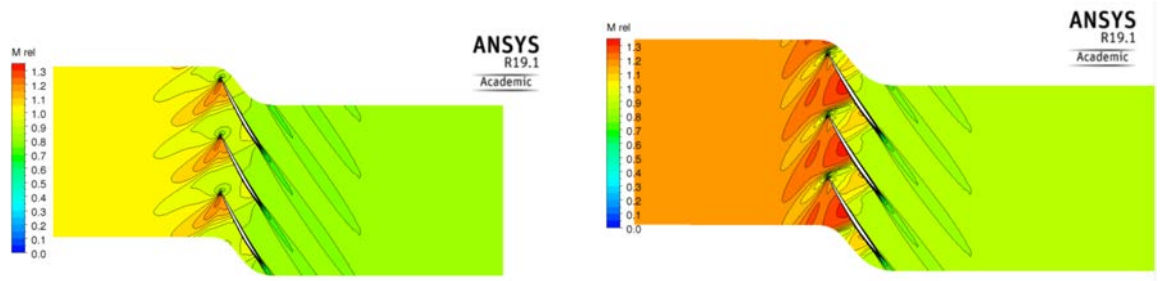

(a) Contours of M_{rel} at 75%

(b) Contours of M_{rel} at 90%

Figure 41: Contours of relative Mach for two different operating point in the compressor map

The previous figure depicts two different blade to blade views at the same span (90%) for two opposite points in the map. It can be worked out how the number increases as the speed line is moved towards the left bottom side of the map. That is explained by the fact that the lower the angular velocity is, the lower the U is, as explained by the equation:

$$\omega = \frac{U}{r} \tag{10}$$

where r is the radius (distance from the hub). Equation 10 also explains why at the tip section the velocity is higher. If U is isolated and ω is kept constant (speed line is not changed) and r is increased (moving toward shroud) the velocity increases. Contrarywise, at the hub, the velocity is the lowest possible; this means that particular attention should be focused on the tip, because of the consequences of high speed flows.

3.4 Full annulus analysis

The simulation with the full annulus, which means the entire 22 blades, is the first important step towards the matching of the transonic fan and the S-duct intake. As a matter of fact, it is not worth it to simulate the single channel downstream of the duct, because the pressure profile is not uniform and, hence, the rotor is differently affected by this pressure's distribution. The struggle is to understand the behaviour of the flow and what it brings about in terms of efficiency and overall performance. All of these aspects will be lately discussed and analyzed. For the moment the attention need to be

focused on the entire fan and the difference that might occur from the single channel simulation.

The two simulations are closely linked, because in both of the cases the incoming flowfield is clean (no distortion is generated), but the problem is the central hole that is created when the full anulus is assembled. For instance when there is the revolution of the blades, the region of the shaft is left blank and this should be avoided.

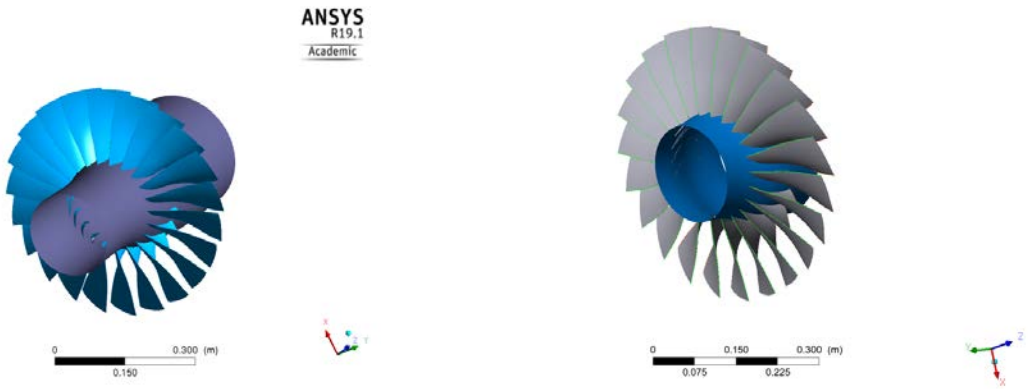

(a) Full annulus geometry of R67 (b) Full annulus geometry of R67 modified

Figure 42: Geometries of the full annulus

The geometry of hub creates a perpendicular wall which might both entail difficulties in the convergence of the calculation and it is not representing the physical behaviour of the flow. Actually, this situation might be accepted for the uniform-inlet-condtion simulation of the full annulus, because the fluid affects the blades equally in every point. Despite of this fact, it was decided to implement an ogive upstream of the fan which has the duty to drive the air from the inlet towards the blades. The attention in designing the ogive was not really focused on its shape; indeed, the purpose was not to develop the nacelle to guarantee the highest efficiency possible. However, the geometry was thought just to gently drive the fluid without any detachment from the wall and to present perpendicularity in the direction of the flow when it encounters the blades. In order to do so, the geometry was drawn on SolidWorks and the mesh was done by using ANSYS workbench. But, before the coupling of ogive and fan the geometry of the latter had to be modified to enable the perfect connection.

The Figure 42b depicts how the geometry is shortened from the initial case of Fig. 42a and, this step is done on TurboGrid in which the control points of inlet and outlet can be easily modified. As for the ogive, the geometrical dimension are known since they must match the fan's ones. Hence, knowing the shroud radius, a cylinder of that dimension was created; consequently the central hole (same dimension of the hub) is

drawn. Finally, the shape of the nacelle is driven by an elliptic equation with the parameters needed. The Fig. 43a and 43b show the geometrical shape of the ogive and its mesh. As it is concerned with the mesh, it was created by imposing the number of elements on the edge of the cylinder. The most delicate part was the one that is next to the inlet of the fan, because the two geometry are not connected by the same mesh but through an interface (it will be lately explained).

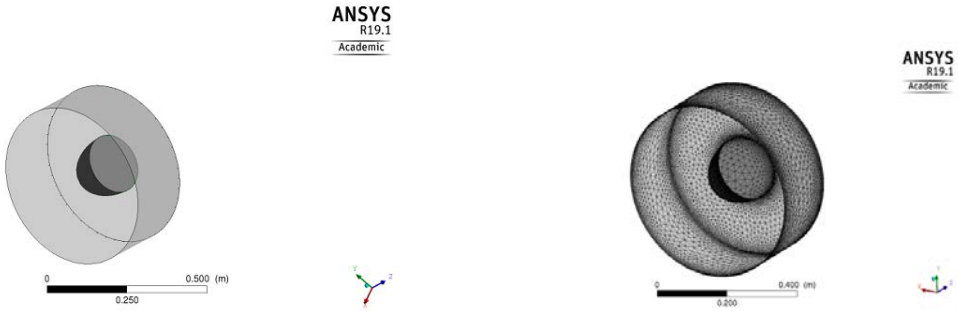

(a) Ogive upstream of the fan (b) Ogive's mesh

Figure 43: Geometries and Mesh of the ogive

Now the challenging aspect is the connection of the two parts, which, obviously do not present the same mesh. Therefore, an interface is created between the outlet of the ogive and the inlet of the fan. The interface might be modeled by selecting three different mixing models:

- Frozen Rotor
- Stage (Mixing Plane)
- Transient Rotor-Stator

In order to match multiple surfaces only one constrained is required: both of the surfaces must be a result of a revolution, plus, they must sweep the same area. In the frozen rotor, the frame is varied without changing the component's relative orientation (during the simulation the two frames remain in the exact relative same position). The drawback of this model is that transient effect are not taken into account as well as the losses that incurs when the flow passes through the interface. Lastly, the computational demand of this model is the lowest possible for the three models. The stage model entails a circumferential averaging along the interface. In this case, steady-state solution are achieve in both of the frame, but, on the other this model is more time-consuming rather than the previous one, but far from the computational costs required for the transient rotor-stator. As it is for the latter model, it should be used when the transient interaction effects at the interface require particular attention.

Furthermore, the pitch change option had to be set to allow ANSYS to implement an algorithm to detect overlapping zones. For instance, this setback happens when the entities are placed in the same domain and they are very close to each other; in addition having different meshes negatively affects this problem and, at the interface might arise overlapping situation, which shoud be avoided. As a matter of fact, the meshes of the ogive and of the inlet of the fan are different, but at the interface plane the ogive's one is intensified to try to better simulate the change of domain. The possible way to select how the pitch is changed are four:

- None, the connection is made "as is" and, indee, if there are overlapping zones the flow is conveyed only in that region. Preferebly to use when the position of the two components perfectly matches.
- Automatic, is usually used when there is the same radial or axial dimension but the extent in the direction of rotation.
- Value, enables to the user to specify the pitch ratio.
- Specified Pitch Angles, allows to impose the angle on both of the sides of the interface.

Finally the mixing model that was assumed is the Frozen Rotor because it was considered the option to run the calculation. Moreover, it was initally set the None option because the geometry were carefully placed one next to other without overlapping any region. However as soon as the simulation started an error was yielded out; in fact the problem is that the algorithm that finds the presence of overlapping regions is failing if there is presence of:

- Surfaces with zero radius
- Surface of constant radius with surfaces of constant z

Therefore, while returning this error, it was suggested to switch the option to Automatic to let the algorithm properly works.

From the Fig. 44 it is clear how the two systems are assembled together and which is the interface between the two components. As a matter of fact, there are three different domains for the simulation:

- Ogive upstream the fan
- Rotor blades
- Outlet downstream the rotor

The ogive is where the inlet boundary condition are set (the same of the isolated single channel rotor of the §3.2). The central part (rotor) receives the condition through the interface and it is mainly concerned with the simulation of the flow through the passage which is the critical step. At the end of the system there is the outlet, which was created just to create a longer outlet domain to better describe the wake effect.

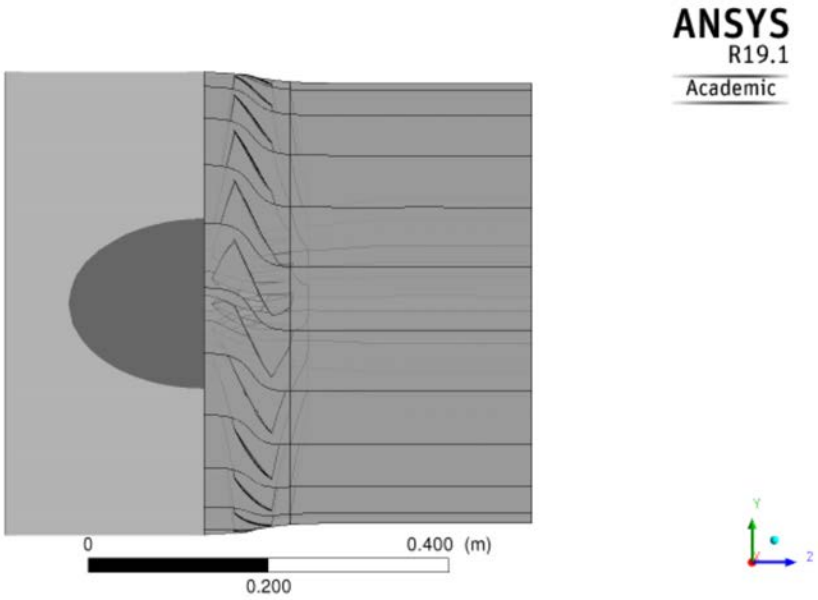

Figure 44: Entire component: ogive upstream plus the fan

For this simulation all the difference between the single channel are analyzed in the following table.

Table 5: Single channel and full anulus simulation features

Simulation	Mesh Model	No. of Nodes	CPU Cost	No. of Iterations
Single channel	Coarse	900k	4 hrs	3200
Full anulus	Coarse	22 mln	14 hours	500

As a matter of fact, as stated before the mesh used is the coarse one because it produced high fidelity results for the single channel with lot of less comutational cost rather than the very fine model. On the other hand, as for the simulation of §3.2 the processor used were 16 (equivalent to 1 node on the cluster of Cranfield University), here the calculations are carried out with 1 node of the cluster. The drawback is related with the computational time required that iss still too much (14 hrs) for one simulation of 500 iterations. For instance, even the number of iterations are reduced otherwise the CPU time was going to explode, and, consequently the precision is not that high of the single channel calculation as it will lately discussed. Even for these

simulation, the entire compressor map is simulated to highlight the differences that in the single channel might not be worked out, such as the distribution of the pressure on the blades of the rotor. Moreover, another aim of simulating the entire annulus is to gently approach the simulation of the S-duct upstream of the fan.
In this case, anyway, the profile of the total pressure at the inlet of the ogive is clean and not distorted.

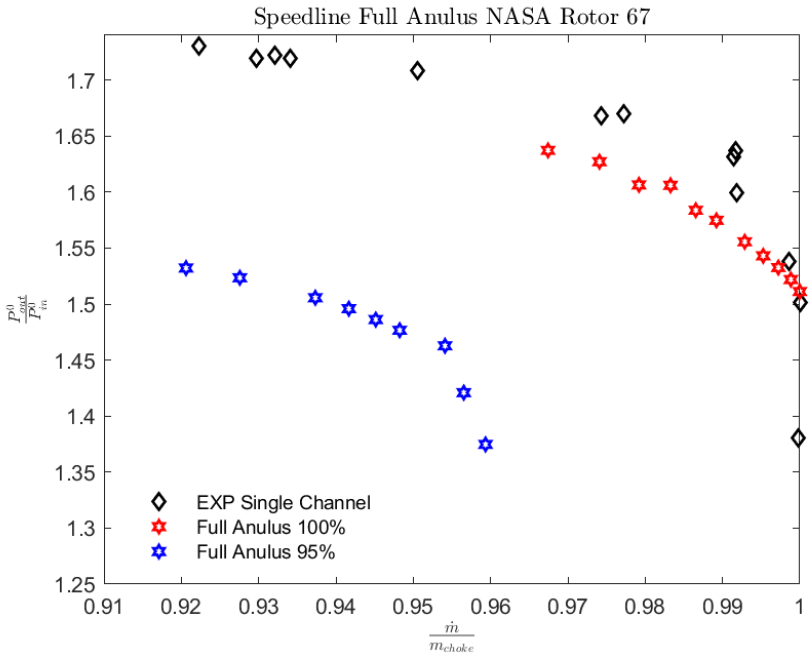

Figure 45: Compressor Map for 100% and 95% of the full anulus

From Fig. 45 the trend of the simulation with the full anulus model are shown, and apparentely, the similarity between CFD and experimental data is very encouraging. The deviation of the CFD results is not that, if it is taken into account that the number of the iterations is more than halved. Moreover, as done for the single channel, the speedline is simulated by varying the back pressure at the outlet, from the choke condition to the surge limit. In addition, even the speedline of 95% of rotational speed is analyzed, since it perfectly matched the requirement for the S-duct intake as it will lately discussed in the next chapter. Lately, the comparison between the two models is drawn in Fig. 46, where the single-channel and full anulus simulation's results are reported. It is clear how the two calculations are not that far from each others as it is seen in the figure. Actually, the speed line at 95% is very close to the single-channel simulation; as a matter of fact the deviation of the two simulations are very tight. From the following table it is possible to work out the main differences in accuracy between the models simulated.

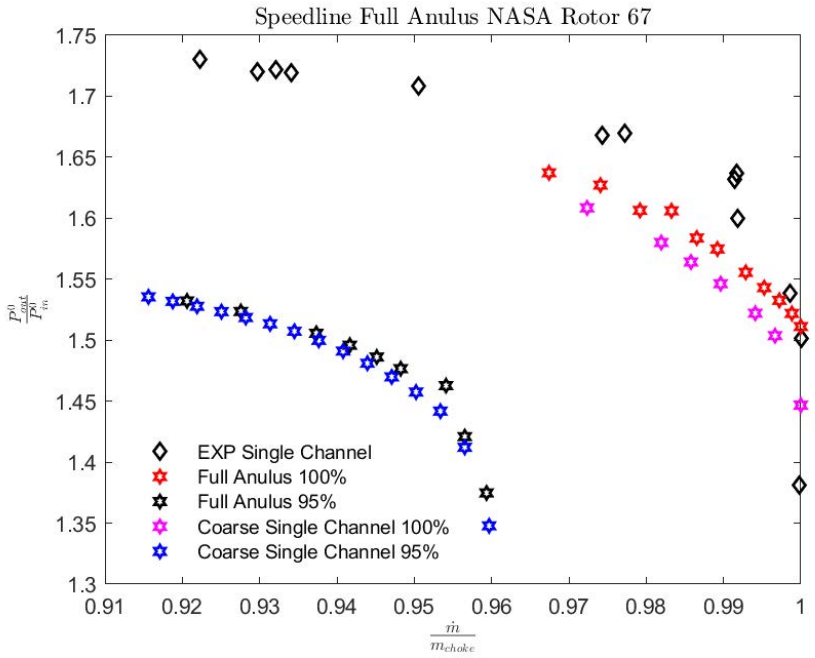

Figure 46: Comparison between single channel and full anulus on the compressor map

Table 6: Single channel and full anulus simulations' comparison (Near Stall)

Simulation	$\dot{m}$ $[kg/s]$	$\Delta\dot{m}$	η_{is}	$\Delta\eta_{is}$
Single Channel Fine	33.2366	-	0.905865	-
Single Channel Coarse	33.2202	$+0.0164$	0.903910	$1.955e-3$
Full Anulus	33.1807	$+0.0559$	0.906602	$-7.37e-4$

Table 7: Single channel and full anulus simulations' comparison (Near Peak)

Simulation	$\dot{m}$ $[kg/s]$	$\Delta\dot{m}$	η_{is}	$\Delta\eta_{is}$
Single Channel Fine	33.4226	-	0.911848	-
Single Channel Coarse	33.4402	-0.0176	0.904349	$7.499e-3$
Full Anulus	33.4088	$+0.0138$	0.907245	$4.603e-3$

Table 8: Single channel and full anulus simulations' comparison (Near Choke)

Simulation	$\dot{m}$ $[kg/s]$	$\Delta\dot{m}$	η_{is}	$\Delta\eta_{is}$
Single Channel Fine	34.2867	-	0.888468	-
Single Channel Coarse	34.2762	$+0.0105$	0.875048	$+0.01342$
Full Anulus	34.2976	-0.0109	0.871416	$+0.013264$

All of the previous tables are useful to analyze how the simulation varies from model to model and how faithfull the simulations are. Since full-annulus analysis have not been found and no experimental data are provided, the reference point is the single

channel with the finer mesh. As it is concerned with the three situations taken into consideration, there is high agreement among the results. Of course, the exact results of the single-finest channel are impossible to be matched. It might be asserted that the difference during the calculation of the mass flow rate is very modest; for instance, every CFD $\dot{m}$ of the entire fan differs of a factor of +0.0559 at maximum. Nevertheless the value might appear not that low, it is easy to think that such deviation entails a relative error of 0.0017%, which is absolutely tolerable. Furthermore, the tables are able to highlight the diversities not only between the single coarse and fine mesh, but also between the two identical meshes but different simulation (single channel vs full anulus). As a matter of fact, as explained in §3.2 the coarse mesh is highly faithfull and here the comparison of $\dot{m}$ and PR testifies that. For instance, the deviation from the reference simulation of the finest mesh is always around ±0.015 as average which brings about a relative error for $\dot{m}$ of 4.4%.

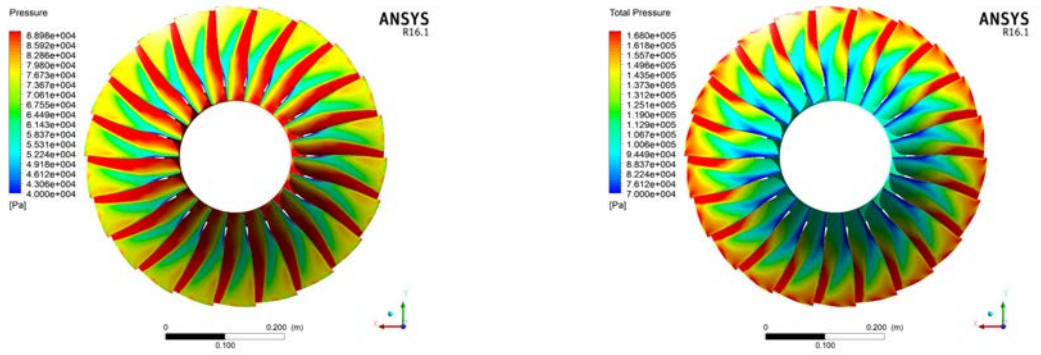

(a) Contours of static P for full anulus simulation (b) Contours of P^0 for full anulus simulation

Figure 47: Near stall contours of static and total pressure for the full anulus simulation

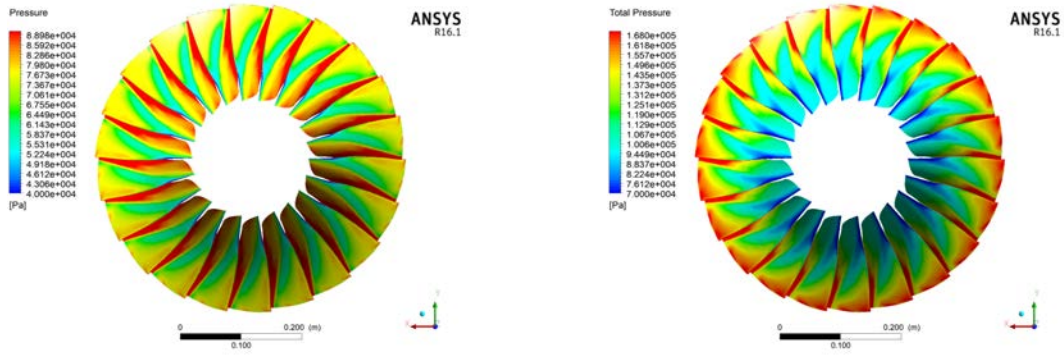

(a) Contours of static P for full anulus simulation (b) Contours of P^0 for full anulus simulation

Figure 48: Near peak contours of static and total pressure for the full anulus simulation

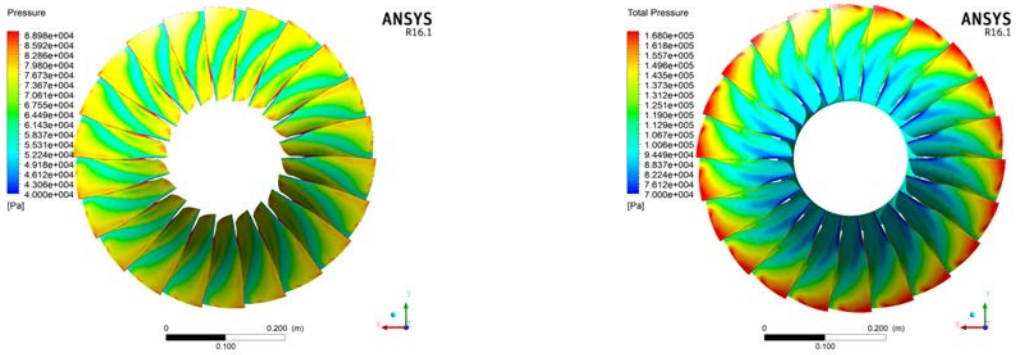

(a) Contours of static P for full anulus simulation

(b) Contours of P^0 for full anulus simulation

Figure 49: Near choke contours of static and total pressure for the full anulus simulation

From Fig. 47, 48, 49 it is possible to observe how the pressure varies from the stall, near peak and finally to the choke condition. As a matter of fact, it is clear how much the blade is loaded for the near stall condition rather than in the choking; that might be worked out by the fact the blades are covered by a wider region with high pressure (red one in this case).

3.5 Full anulus analysis 95% of rpm

As before stated, a simulation with the full anulus model is implemented. This was necessary due to the incompatibilities that were occuring while assembling the S-duct intake and the full anulus. For instance, as soon as the simulation was launched an error of non convergence was detected and the calculations were stopped. Therefore, it was thought to reduced the rotational velocity to avoid this and it brilliantly worked. However, it will be lately discussed in the next chapter about these details. As it is regarding this simulations, the parameters were identical of the 100% model, apart from the ω, that instead of being 16043 $[rpm]$ was of 15240.85 $[rpm]$. The results in terms of overall performance (η and PR) are depicted in Fig. 45, 46. As it is shown, the mass flow rate of the speedline of 95% is lower than the normal speed, plus there is a lot of agreement between the single coarse channel simulation and the full anulus. As a matter of fact the deviation is tighter than the 100%, which might probably be due to the higher stability of the simulation.

Chapter 4

S-duct and R67 Simulation

In this chapter it is explained how the simulation of the entire system is set up. As a matter of fact, the main purpose of the research work is concerned with the understanding of how the intake and the fan downstream of it might interact each other. For instance, since the intake is an S-duct and a curvature is embeeded in the geometry the flow is not clean; it is said to be distorted and the typical distribution of pressure is the one shown in 25a. It is clear how the geometry itself create a zone in which the loss in total pressure is consistent. Three different simulation were carried out:

- S-duct baseline with fan downstream of it
- S-duct optimized (*cp* and DC_{60}) with fan downstream of it
- S-duct optimized (*cp* and swirl) with fan downstream of it

Before further continuining an important aspect should be highlighted; the geometry of the baseline of the S-duct along with the geometries of the optimized intake are taken from [12], in which, in reciprocal agreement, the adaptation and the optimization were carried out.

4.1 Inlet Distortion

During this chapter the situation of inlet distortion is under investigation, in order to understand how it might affect the overall performance of the fan. Furthermore, the curved shape of an S-duct, that creates this situation, damages the stability of the fan and it should be taken under important consideration for the next-generation of BLI aircraft [25].For instance, three are the main inlet distortion pattern:

- Velocity inlet distortion related with the swirl
- Total pressure distortion due to the losses of friction on the wall
- Total Temperature

These three types have diverse textures, which means that they appear in different ways. For example the swirl distortion is concerned with the non-axiality of the velocity. Therefore, the velocity at the inlet interface present an angle in front of the blade.

As it is concerned with both the total pressure and temperature distortion, they are considered to be radially or circumferentially distributed at the inlet of the fan. As stated in [23] the condition in which the flow is considered clean (any type of distortion occurs)is the one of most convenience for the design of the fan. Despite of this fact, the reality proves that the rotor barely faces this situation, and the flow and its properties are not considered uniform. As a matter of fact the inlet is always experiencing disturbed condition. This situation is affecting the performance in terms of pressure ration, isentropic and polytropic efficiency. Naseri et in [23] analyzed that "Inlet distortion patterns redistribute flow parameters over the compressor blades which could in turn alter the stability condition of the compressor and trigger rotating stall or surge". Due to the challenge in considering this aspects, many studies have been carried out with special attention in pressure and swirl distortion. Lots of these works, including [23] and [16] draw the conclusion that the swirl entails different consequences to the performance of the rotor:

- Co-rotating bulk helps to improve the stability of the compressor
- Counter-rotating bulk brings about a decline in the stability

Moreover, both [16] and [23] explained how the swirl and the total pressure distortion coexist at the same time, even if they are usually treated not at the same time. In this work both of them are concurrently considered in order to represent as faithfull as possible the phenomenon.

4.2 DC_{60}

This parameter should be rapidly discussed, since it is one of the two objectives to be minimize in the optimization of the S-duct. It is considered as a useful descriptor for total pressure distortion; for instance it is called sectional distortion coefficient. The definition of this parameter is:

$$DC_{60} = \frac{\bar{P^0_{aip}} - \bar{P^0_{60}}}{\bar{q_{aip}}} \tag{11}$$

in which $\bar{P^0_{aip}}$ is the average total pressure of the AIP, $\bar{P^0_{60}}$ is the average total pressire in each region of 60 and $\bar{q_{aip}}$ is the average dynamic pressure. As it is stated in [2] the DC60 engine face distortion descriptor is a measure of the difference between the engine face or AIP average total pressure and the lowest average total pressure in any sector defined by a critical angle of 60, divided by the average dynamic pressure at the engine face.

4.3 Baseline review and parametric analysis

In order not to create from scratch the geometry of the S-duct intake, the Delot baseline presented in [14] is taken into consideration as starting point. The problem is that the shape is not supposed to be used for practical purposes, but just to analyze how the CFD codes might describe the real phenomenon studied by Wellborn. In agreement with [12] it is decided to adapt the initial geometry to the dimension of the fan, in order to try to assemble the two machine together. Another challenging aspect is the understanding of the initial condition to be set up for the simulation. As a matter of fact, Delot used 88744 $[Pa]$ as inlet condition for the S-duct, but, this condition is not feasible with the requirement of the rotor. This problem is overcome in [12] by a parametric study of the intake; for instance, the pressure needed from the fan to be efficiently operative is 101325 $[Pa]$. The parametric study is easily carried out by varying the inlet total pressure, in order to match, as accurately as possible, the area-weighted-average total pressure at the outlet of the intake. To do so, the outlet static pressure is provided by the full annulus model. Once the study is ended the total pressure as inlet condition that satisfy the requirement is set to 106390 $[Pa]$, which brings about a total pressure as inlet for the rotor of 101341.08 $[Pa]$ and actually, it is very close to the one expected and needed.

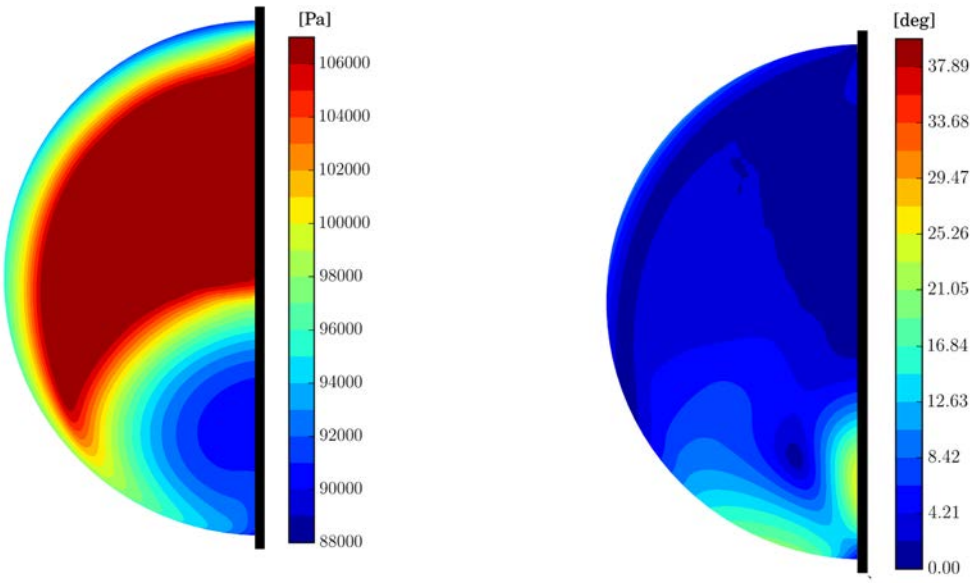

(a) *cp* (b) Swirl

Figure 50: *cp* and swirl representation of the adapted baseline

Fig. 50 depicts the baseline results for the adapted geometry, which are utterly similar to the one in Fig. 25, which shows the Delot baseline's results. For instance, the great agreement of the two identical geometry (with different dimension), plus the correct condition at the outlet of the duct is encouraging to pursue the matching of the two component. However, even if the behaviour is almost identical, the pressure recovery factor is way different for the small and the adapted baseline. Firstly, the pressure recovery factor, *cp*, is a parameter with which the losses in total pressure are calculated. Indeed, the coefficient is expressed by the following equation:

$$cp = 1 - \frac{P^0_{out}}{P^0_{in}} \tag{12}$$

in which P^0_{out} is the total pressure at the outlet interface and P^0_{in} is the total pressure at the inlet of the duct.

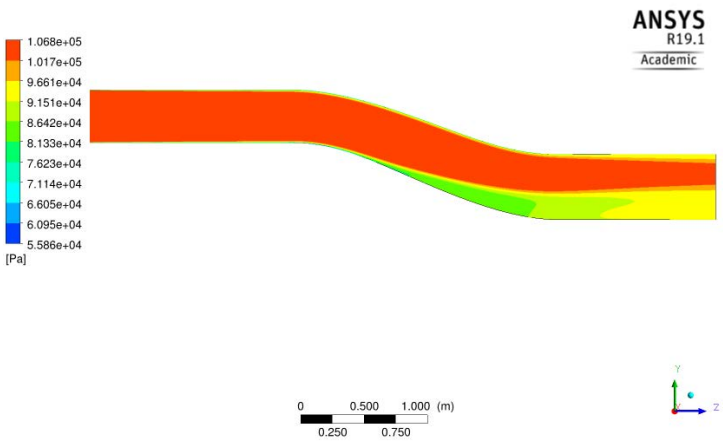

(a) Total pressure

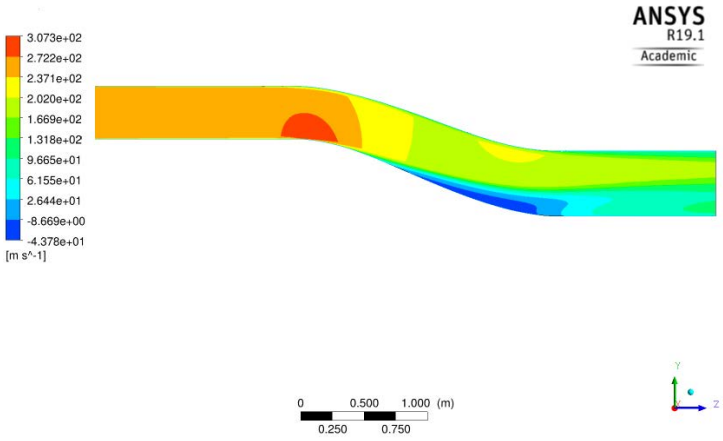

(b) z-velocity

Figure 51: Total pressure and z-velocity on the symmetry plane representation of the adapted baseline

The previous figure shows the symmetry plane, in particular the behaviour of the total pressure and of the z-velocity. As for the Fig. 51a the trend of the P^0 along the duct reflects the one of the Fig. 50a in the other plane. Moreover, the velocity in 51b depicts an intersting behaviour; as a matter of fact, there is a bubble near the curvature of the duct in which the Mach number is approximately 0.99 (no shock waves occur). After the bending, the velocity decreases and the growth of the boundary layer starts. This happens because the geometry does not allow the fluid to remain attached to the wall; the velocity in blu is negative, which underline the recirculation of the flow in that region.

Table 9: Delot and adapted baseline comparison

Individual	cp	$\alpha[deg]$
Delot Baseline	0.0310	3.3978
Adapted Baseline	0.048042	4.73329

From the table 9 it is possible to work out the main differences between the two simulation. Nevertheless the geometry is the same, but the dimension are not, the swirl angle and pressure recovery are highly different; this might be explained since the boundary condition has drastically changed.

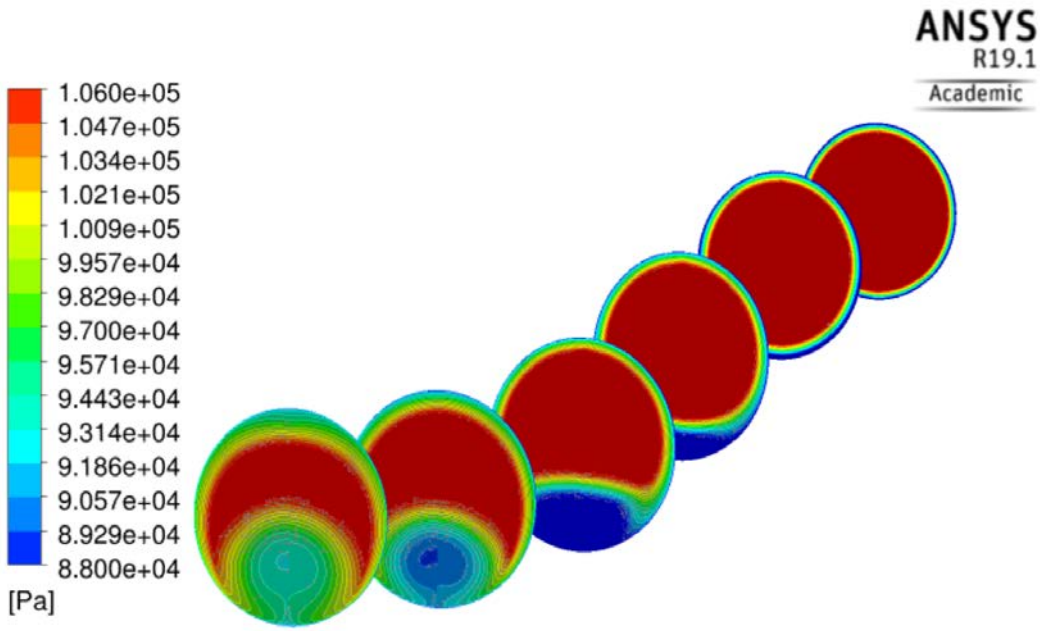

Figure 52: Isometric view of total pressure in different plane

The Fig. 52 shows how the isometric view of the S-duct from inlet to outlet, and, in particular how the distribution of the total pressure varies along the duct.

From a uniform condition at the beginning, in which the profile is all red with a tiny blue circle, which highlights the friction losses at the wall, to the outlet in which the profile is highly distorted, and the plane is divided into two different region; the first one is ruled by an high pressure (red) and the latter is the blue region in which the pressure suffered a considerable drop. This non equilibrium of distributon in the pressure field entails the non axiality of the velocity, but, despite of this fact, the average pressure at the interface between S-duct and fan is the one required for the correct condition of operability.

4.4 S-duct and rotor R67 interaction

This section is dealing with the most challenging step of the work of research; for instance,the assembly of the intake and the rotor is not been widely studied in literature. As a matter of fact, the majority of the works are related with inlet distortion automatically generated, by giving an angle of distortion and, most of all, without considering the swirl angle. As before stated, the simulation is thought to be as faithfull as possible and, therefore, both the pressure distortion and the swirl are considered. The entire simulationis carried out on CFX, by exploiting the cluster of Cranfield University. In this case, differently from the previous ones, the simulation is carried out by using multiple nodes in parallel. This is due to, to the heavy computational cost, that the simulation required. Indeed, the parameters of the simulation are:

- No. of Nodes 23e+6
- No. of Domains 4
- no. of Iteration 1500
- No. of CPU 64 cores
- Computational cost 15hrs

Since the calculations is highly time-demanding it is decided to simulate just one speed line, and not the entire compressor map; the speed line that is taken into account is the 95% of the rotational speed. This, because with the angular velocity at its maximum value, the simulation is highly unstable and problems of convergence arises. The domain is split into four different body and then connected with the property of interface in CFX. In Fig. 53 the system is depicted and all the four parts are visible. The first domain is the intake, in which the inlet boundary condition are set; after that the ogive is placed to kindly drive the flow from the duct to the blades.

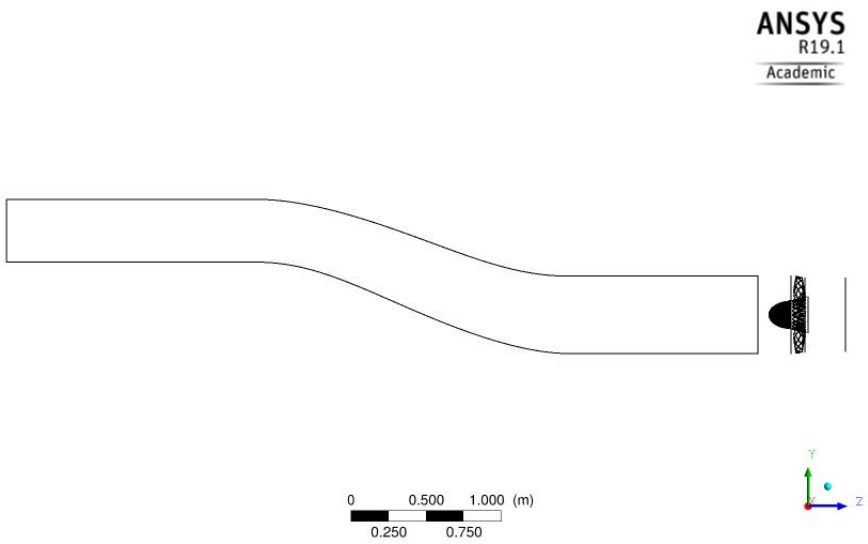

Figure 53: View of the entire system

The blades represent the third domain in which the rotor does its work; indeed the pressure boosts dramatically. Finally, the last part is the outflow, where the outlet boundary condtion are given and its function is to create a region in which the fluid is as uniform as possible. The calcultation of the S-duct in [12] are done on half of the geometry in order to save CPU time, here, it is impossible because the fan might be affected differently. Therefore, the geometry has been revolved to complete the entire duct for the simulation as it is shown in Fig. 54.

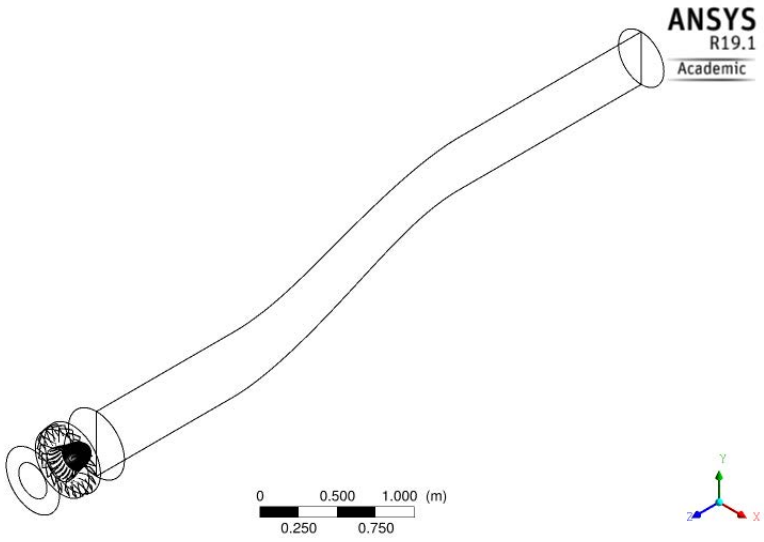

Figure 54: Isometric view of the entire system

The interface among the components of the system are modeled in the same way of the interface for the full annulus simulation. As for the inlet condition, the total pressure is given and in particular the value set is the one carried out in [12] during the parametric analysis of the intake and it is of 106390 $[Pa]$. For instance, the outlet condition is varied every simulation due to the will to study all the speed line (from the choking asymptote to the stall margin).

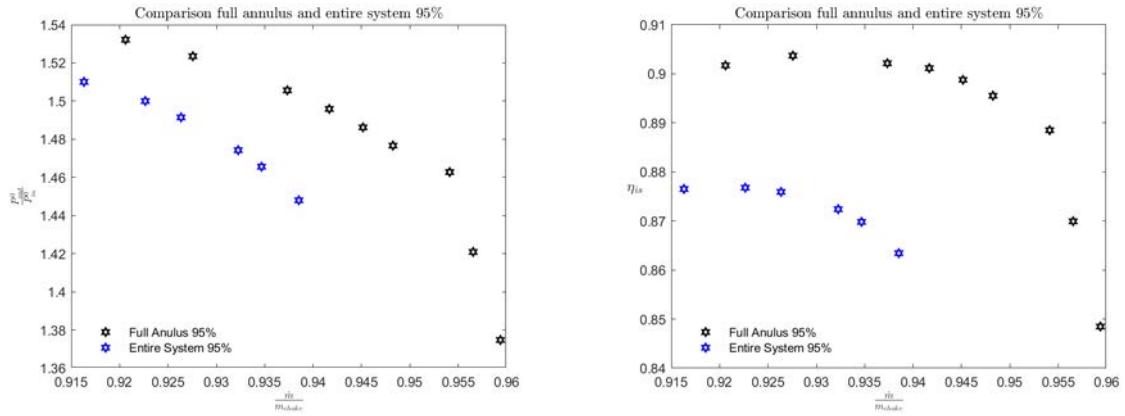

(a) Speed line

(b) Efficiency

Figure 55: Overall performance comparison of the entire system and the isolated full annulus

The Fig. 55 shows the overall performance of the entire system with respect of the full annulus model. Many observation might be done:

- The trend of the speed line is preserved, even if there is tight deviation from the results
- The trend of the efficiency is almost the same; the η_{is} in the distorted inlet flow is deteriorated

Table 10: Full annulus and entire system comparison

Model	$\dot{m}[kg/s]$	Rel. Error	η_{is}	$\Delta\eta_{is}$
Near Peak Clean	32.7692	-	0.902150	-
Near Peak Distorted	32.2559	0.015 %	0.876780	-0.025
Near Stall Clean	32.1846	-	0.901716	-
Near Stall Distorted	32.0346	4.7e-3 %	0.876521	0.025%

Table 10 expresses the comparison between the two simulation, and it tries to quantify the relative error between the clean and distorted simulation. As it might be seen, the deviation on the mass flow rate computed in the two models is not that wide;

for instance, near peak the entire system brings about a relative error of 0.015%, which is absolutey tolerable. As it is concerned with the isentropic efficiency, the reduction is quite high; this is an indicator of how the performance is deteriorated in the simulation with the rotor downstream of the S-duct. This drop in the efficiency is entailed by the non uniform pressure distribution along with the the non axiality of the flow at the inlet of the fan. The following pictures help to understand where the distortion occurs and how the properties are distributed along the blades. In particular, it will be taken into consideration the four condition of table 10.

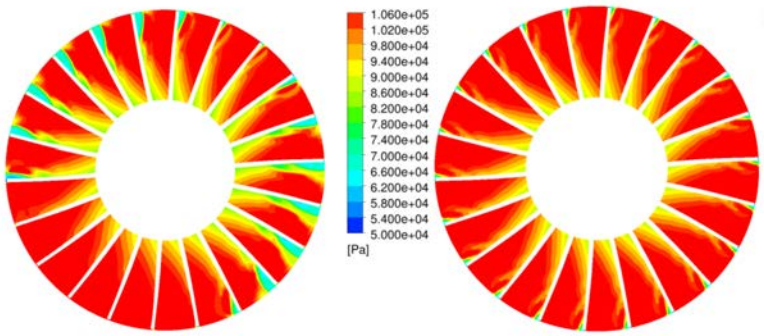

Figure 56: Pressure contours for clean and distorted model near stall condition

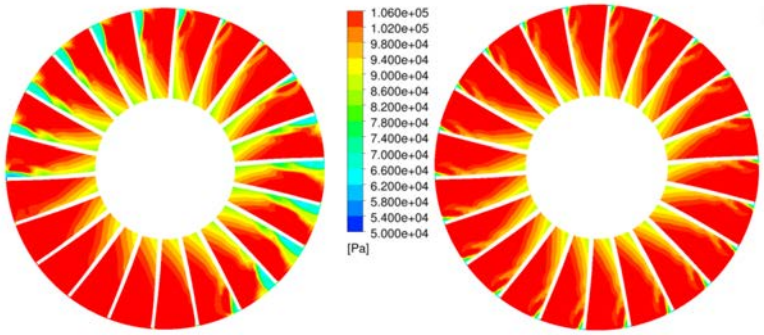

Figure 57: Pressure contours for clean and distorted model near peak condition

On the right the static pressure contours for the full annulus simulation with clean flow is shown for both near peak and near stall conditions. In this case the behaviour of the pressure is symmetrical on all the annulus, since no distortion occurs during the simulation. Moreover, the region near the tip is featured with a small region of low pressure coloured in light blue which is linked with the highest velocity region of the blade. On the other hand, in the Fig. 56a and 57a the entire model's pressure contour

is shown and it is clear how the symmetry is not respected. As it is expected, due to non-uniform pressure gradient at the outlet of the duct, the fan has to face region in which the pressure is not symmetric and therefore, blades are differently affected.

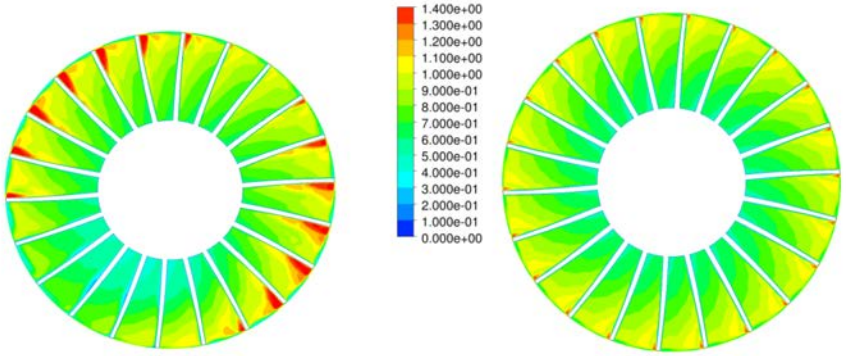

Figure 58: Mach contours for distorted (left) and clean (right) model near stall condition

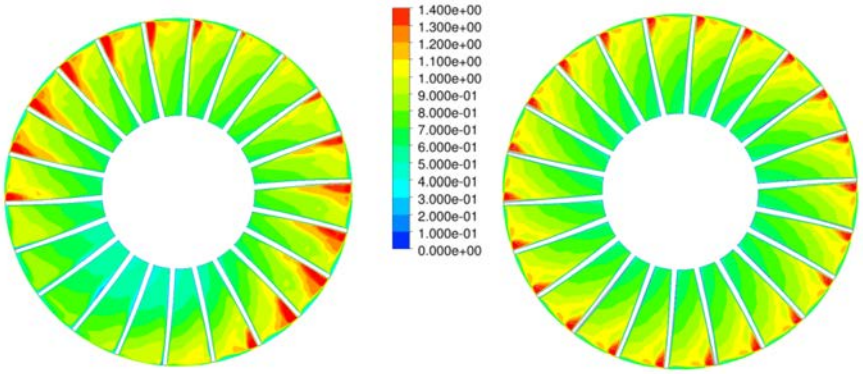

Figure 59: Mach contours for distorted (left) and clean (right) model near peak condition

The figures above display the trend of the Mach number in the same plane of 56 and 57 for both of the model. Comparing the plots for the same operating point respectively (near stall or near peak), a high agreement is detected; for instance, the trend of the static pressure precisely reflect the behaviour of the Mach in the same plane. In fact, whenever the number of Mach crosses the sonic value of 1 (from yellow to green), a shock wave appears in the same position in the pressure contours. Finally, the last results that are reported is the contour of the static pressure calculated directly on the blade. In this way, it is possible to better appreciate how the pressure is ditributed along the span and how the distortion is developing. The two figures (60 and 61) depicts the variation of static pressure through all the blades of the full anulus; for

instance many considerations might be done. Firstly, it is clear how the fan is working with higher pressure in the near stall condition, as it is expected, and this is highlighted by the wider red region on the blades. On the other hand, this trend is not that visible in the distorted model but, despite of that, the region of higher pressure is more spread.

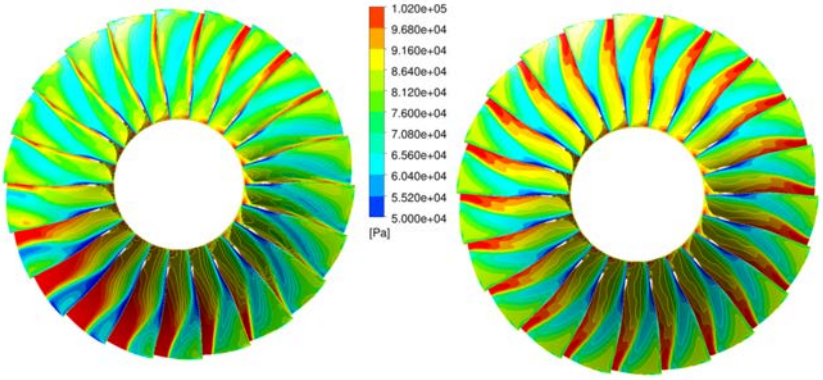

Figure 60: Pressure contours on the blade near stall condition

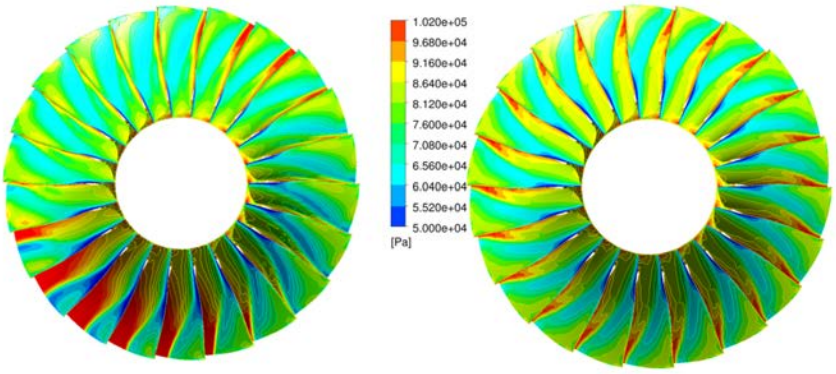

Figure 61: Pressure contours on the blade near peak condition

Finally, in order to sum up the baseline results' discussion compared to the clean flow, it might be said that:

- The distortion due to the presence of the intake is visible in the plot reported before
- The distortion is located on the left lower part of the rotor in all of the simulations
- The trend of Mach number, static pressure both in the middle plane and on the blade are utterly in agreement each other
- The overall performance of the rotor are deteriorated due to the presence of the duct, and it is possible to notice from the Table 10

4.5 Optimization (DC_{60}) of the S-duct's results

In this section the results of the optimization carried out in [12] are reported, and, with particular interest how the optmized geometries might improve the overall performance of the rotor. For instance, the optimization is drawn to enhance the possibilties of the intake to reduce the losses of total pressure and to decrease the level of distortion at the interface of the two components. As a matter of fact, a multiobjective optimization is set up, with the model MOTS (Multi Objective Tabu Search) in which the target to be minimized are the pressure recovery (cp) and the DC_{60}. The first one is linked with the reduction of the distortion of the total pressure and it is computed as stated in §4.3, while the DC_{60} is related to the non axiality of the flow. The optimizaztion process lasts almost a week bringing about optimal improvement, with which carrying out the comparison with the baseline.

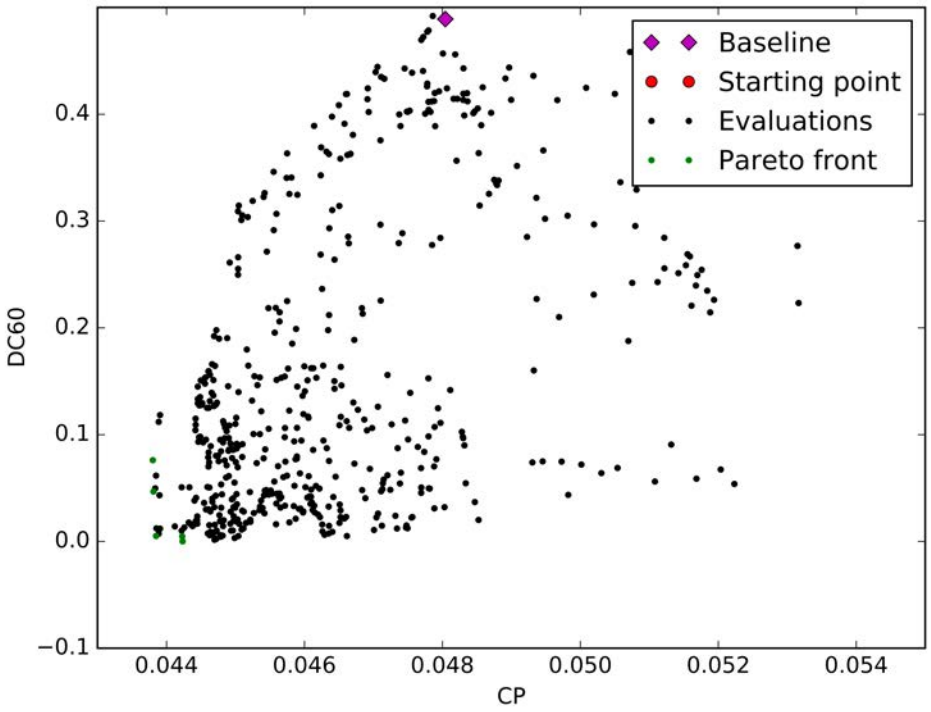

Figure 62: Pareto front with DC_{60} as objective function [12]

The figure shows the Pareto front of the optimization and it is clear how much both of the objectives are highly decreased. In order to understand which might be the effect of those new geometries, three different simulations are set up. As a matter of fact, the best individual both for cp and DC_{60} are taking into consideration; plus a trade off geometry is choosen. Furthermore, the simulations are carried out only for the near peak condition, due to a high computational cost for the entire speedline for

the three different geometries. The following pictures are meant to make understand how the algorithm changed the geomtry in order to get better results.

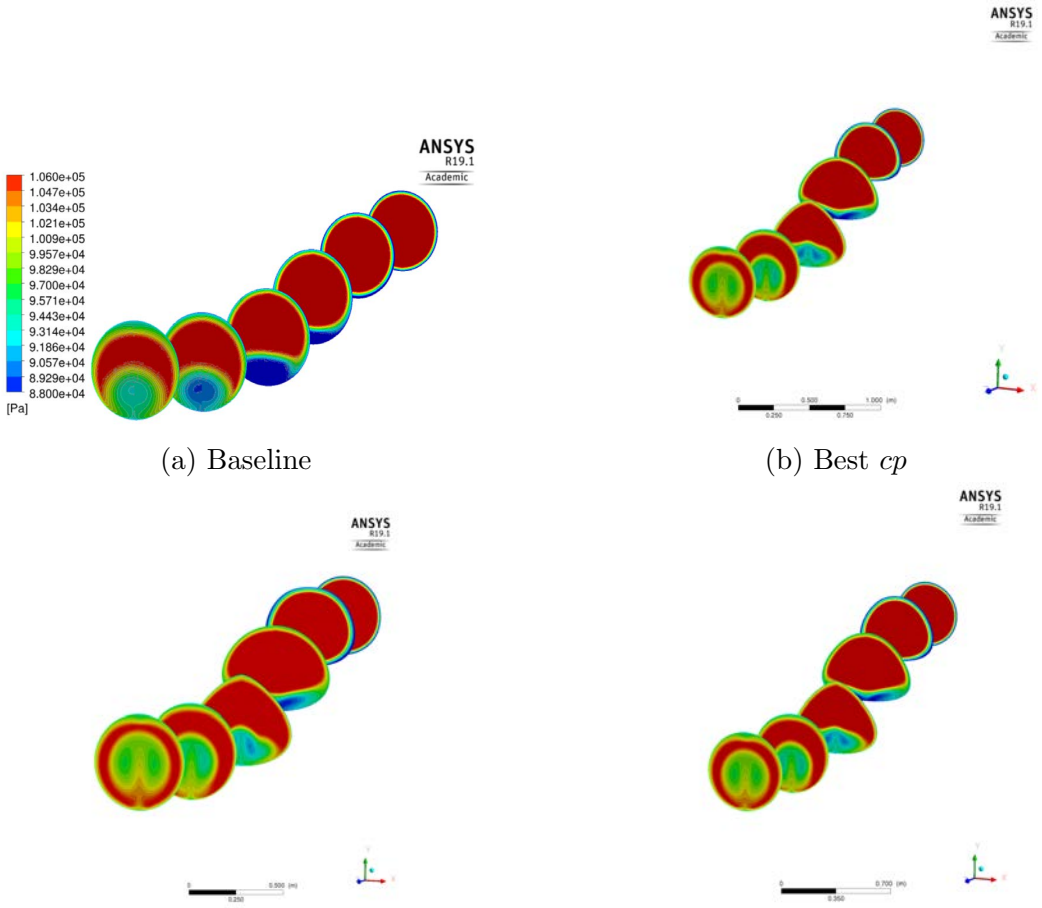

(a) Baseline

(b) Best *cp*

(c) Best DC_{60}

(d) Trade-off

Figure 63: Baseline and optimized individuals geometries' comparison

From the above pictures, the changing in the geometry is clear; the shape is not drastically changed on the plane y-z, but this happened in the x-y plane. For instance, the cross-section is no more circular, but it collapse into different shapes (either elliptical or almost triangular) as soon as the curvature occurs. This is justyfied by the fact that the optimization can vary the geometry only in that part; the inlet and the outlet are left fixed. The outlet total pressure distribution is slighly different from the baseline one; in fact, the higher pressure is ditributed at the outer part of the section, which could be good if it is considered that the blades of the rotor are in that position. Moreover, the profile is literally improved with respect to the baseline because the region in which the pressure's drops occurs is not only reduced, but also is featured with a high value of average pressure.

Table 11 reports the results for the geometries considered in terms of *cp* and DC_{60}. Before from the Fig. 62, but even now it is possible to understand how the intake has

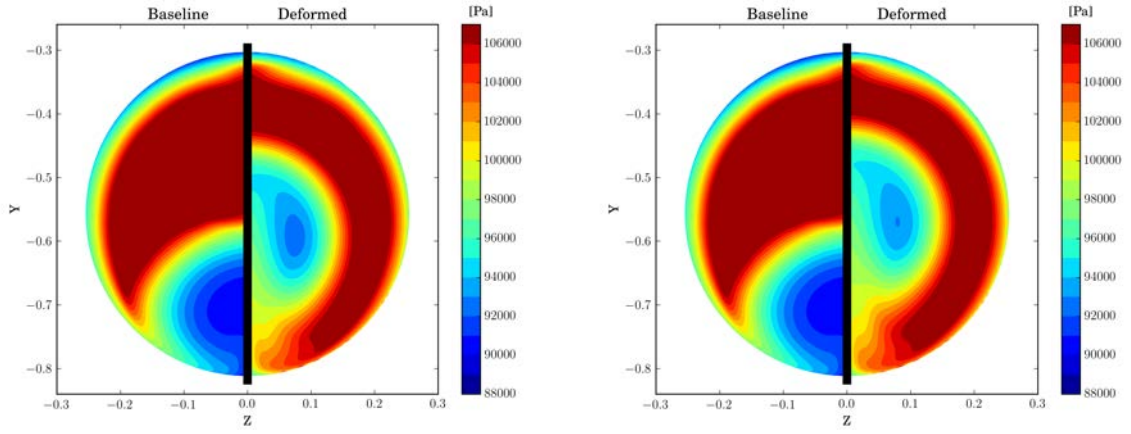

(a) Baseline and Best *cp* [12]

(b) Baseline and Best DC_{60} [12]

Figure 64: Baseline and optimized individuals total pressure comparison [12]

been improved in [12]. As a matter of fact, the DC_{60} has been decreased from an initial value of 0.48912 to 0.00167 at maximum, whilst the *cp* from 0.04804 to 0.04380 for the best individual.

Table 11: Optimization (DC_{60}) individuals comparison

Individual	*cp*	DC_{60}
Baseline	0.04804	0.48912
Best *cp*	0.04380	0.07611
Best DC_{60}	0.04423	0.00167
Trade-off	0.04384	0.00507

Table 12 reports the comparison of the performance among the baseline and the optimized geometries for the near peak condition. From its analysis it is clear that in all of the three optimized models the polytropic efficiency is improved, which means less losses from the rotor. The comparison among the π_c is meant only to highlight how close are the results of the simulations. This optimization brings about that the less the *cp* is, the higher the η_{pol} increases.

Table 12: Performance of the optimized geometries DC_{60}

Individual	π_c	Rel. Error	η_{pol}	$\Delta\eta_{pol}$
Baseline	1.50000	-	0.885606	-
Best *cp*	1.49336	4.40e-3 %	0.890612	+5.00e-3
Best DC_{60}	1.49573	2.85e-3 %	0.890460	+4.85e-3
Trade-off	1.49327	4.48e-3 %	0.890584	+4.90e-3

The Fig. 64 is related with the comparison of the distribution of the total pressure. The previous consideration are valid for this picture as well, since the aim of 64 is only to better depicts the distribution.

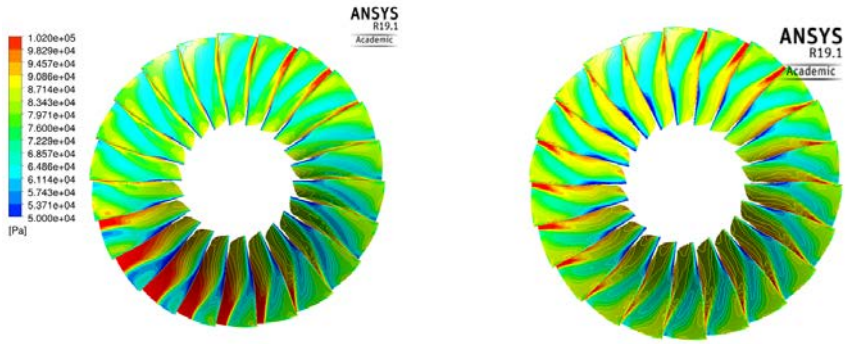

Figure 65: Baseline (left) and best DC_{60} (right)

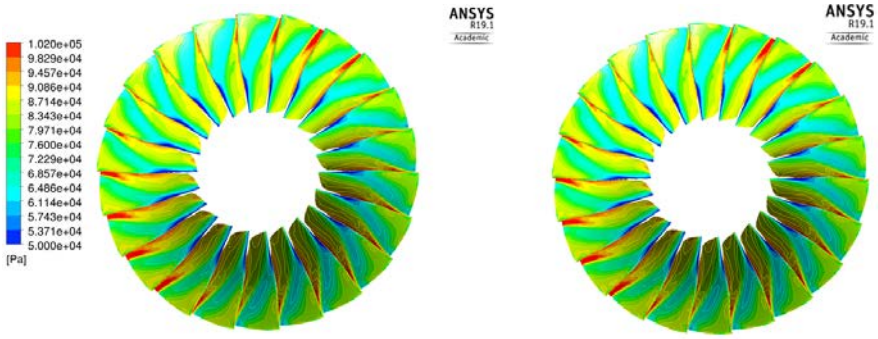

Figure 66: Best *cp* (left) and trade-off (right)

Analyzing the previous figures, it is possible to work out how optimization process has decreased the distortion of the pressure. As a matter of fact, by comparing the baseline static pressure contours with the optimized geometry, the red region on the lower left part of the anulus is highly decreased; for instance, the distribution is total pressure is still distorted, but the level of distortion is utterly lowered. This aspect affects the efficiency of the fan as well; in fact, as stated before, in all of the optimized geometries the η_{pol} is increased.

4.6 Optimization (Swirl) of the S-duct's results

As for the previous section, in this one, the results of the second optimization are discussed. In [12], in reciprocal agreement, a different process of optimization is set up; in this case the objective function are the pressure recovery factor and the swirl angle. The latter one is related with the non axiality of the flow, and it is an indicatore of the angle of which the velocity is distorted. Therefore, after having analyzed these results, a comparison between distortion parameters (DC_{60} and α) is drawn. The process in which the simulation is run, are totally similar to the one of §4.5, and the time of the simulation lasts approximately one weeek.

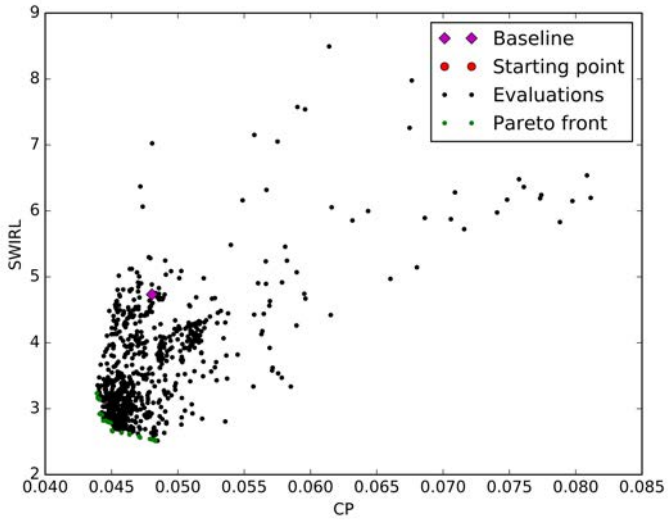

Figure 67: Pareto front with α as objective function [12]

The Fig. 67 shows the Pareto front of the optimization for the swirl angle and *cp*. In this case, the front is more populated with respect of Fig. 62, but, on the other hand, the improvement of α is not that striking as the one for the DC_{60}. As for the pressure recovery factor, the optimized geometries present similar values with respect of the previous ones. Even in this simulation it is clear in which direction the algorithm is looking for new individuals, but there is a difference fromt the optimization in §4.5. For instance, in this case the baseline is improved with all the Pareto's points, but not for both of the objectives, as it happened in the previous one. For the comparison with the baseline, since the front is well-populated, it is choosen to simulate four different geometries anf to compare the results among each other, but also with respect to the improvement of the first optimization. Therefore, either the best *cp* and α are selected or two trade-off individuals near the two extremely conditions. The geometries plus the distribution of the total pressure along the S-duct intake are shown in Fig. 68.

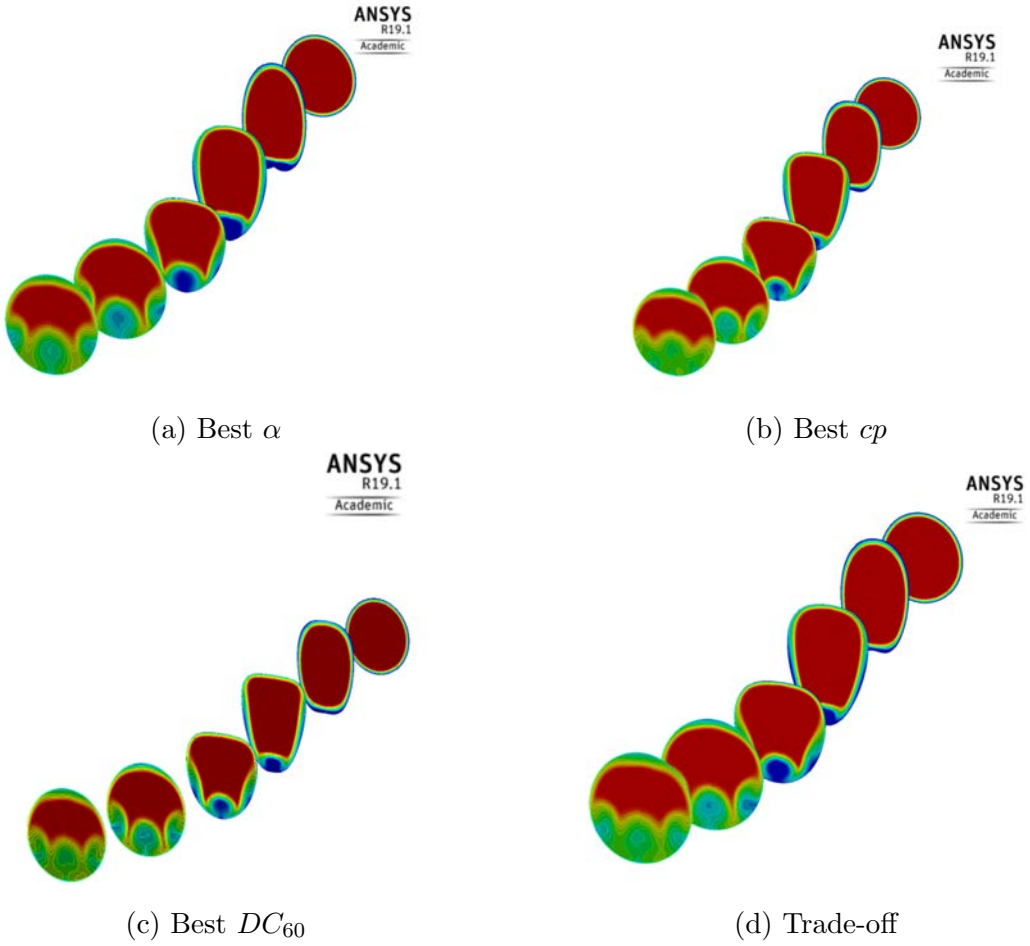

(a) Best α (b) Best cp

(c) Best DC_{60} (d) Trade-off

Figure 68: Baseline and optimized individuals geometries' comparison

The comparison with the baseline in Fig. 63a depicts that the geometries are highly deformed as well. As a matter of fact, the cross-section is no more circular, but it varies along the curvature to minimize the two objectives.

Table 13: Optimization (α) individuals comparison

Individual	cp	α
Baseline	0.04804	4.73329
Best cp	0.04389	3.23356
Best α	0.04829	2.51120
Trade-off (α)	0.04707	2.58174
Trade-off (cp)	0.04422	2.91428

The previous table hihglights how in [12] the results are improved to permit the fan to operate in the best condition possible. From the comparison of Table 11 and 13, it is clear that the pressure recovery factor has been better decreased in the first optimization. Plus, it is of oustanding interest to understand if it is more convenient to try to

lower the DC_{60} or the α.; as a matter of fact, this is the aim of the second optimization. Fig. 69 depicts the comparison of the pressure distribution for the optimized geometry,

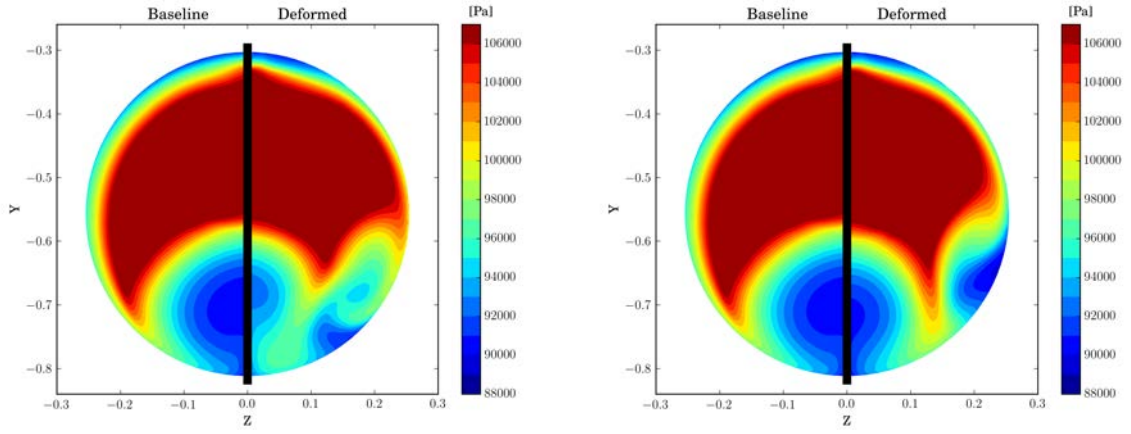

(a) Baseline and Best *cp* (b) Baseline and Best α

Figure 69: Baseline and optimized individuals total pressure comparison for the second optimization [12]

with particular interest on the extreme condition. As it is possible to notice, the profile is very different from the ones that were found in the previous optimization. Instead of having a circular region of high pressure, they are more resemble to the baseline's total pressure distribution. The swirl in the optimized geometries (see Fig. 70) is utterly

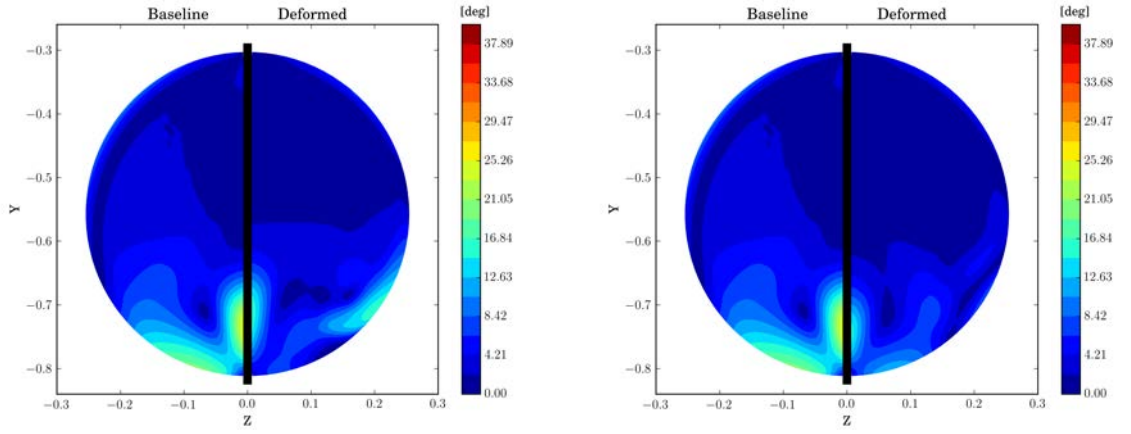

(a) Baseline and Best *cp* (b) Baseline and Best α

Figure 70: Baseline and optimized individuals swirl distribution comparison for the second optimization [12]

lowered, and the flow is characterize by more uniform properties and axiality in the direction of motion.

Table 14: Performance of the optimized geometries α

Individual	π_c	Rel. Error	η_{pol}	$\Delta\eta_{pol}$
Baseline	1.50000	-	0.885606	-
Best *cp*	1.49721	1.86e-3 %	0.888358	+2.75e-3
Best α	1.50323	2.15e-3 %	0.887988	+2.40e-3
Trade-off (*cp*)	1.50006	4.00e-5 %	0.889976	+4.37e-3
Trade-off (α)	1.50393	2.62e-3 %	0.888312	+2.76e-3

Table 14 reports the comparison of the performance among the baseline and the optimized geometries for the near peak condition. It is clear that in all of the four optimized models the polytropic efficiency is improved, which means less losses from the rotor. The comparison among the π_c, as before stated, is only used to quantify the deviation of the results. Morever, in this optimization the best improvement is given by a trade-off element and in particular the one next to the best *cp*. As a matter of fact, the increase in the polytropic efficiency is of 4.37e-3, that is comparable to the improvement reached in §4.5. Furthermore, the distortion in the pressure distribution on the blades of the rotor is expected to be located in the lower left part; this, due to the fact the profile in Fig. 64 depicts the outlet of the intake.

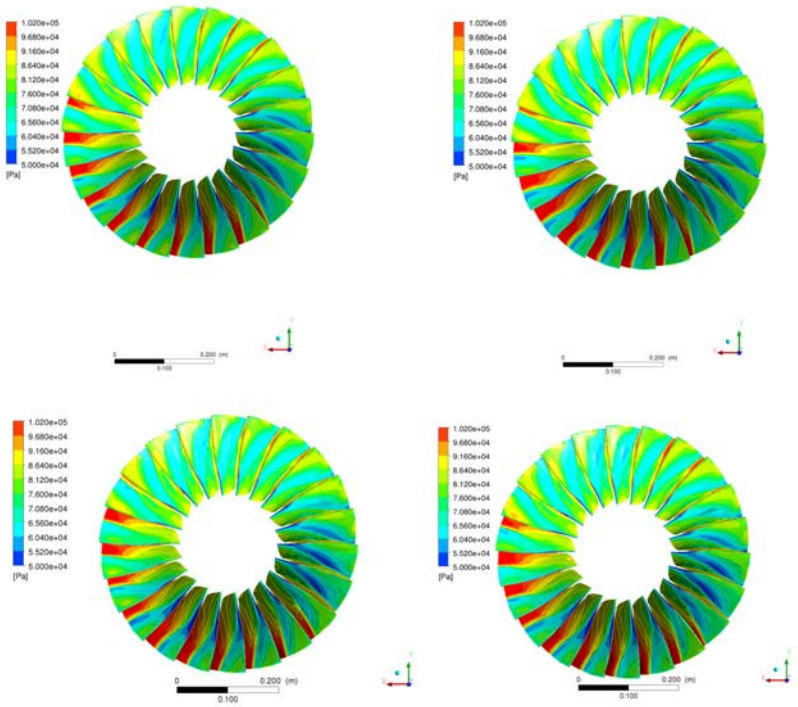

Figure 71: Static pressure distribution for the four optimized geometries: best *cp* upper corner left, trade off near *cp* upper corner right, best α lower left corner and the trade off near best α right lower corner

Comparing the four geometries of this optimization with the baseline in Fig. 66 it is clear that the distortion is still present in the blades, even if it is less consistent than the original shape of the S-duct. MOreover, the pressure distribution is less spread in the case of the trade-off near *cp* individual, and this aspect, is linked with an higher polytropic efficiency rather than the others. Finally, many conclusions must be done:

- Both of the optimizations and the new geometries produce results better than the baseline as it concerned the efficiency
- The first optimization creates geometries with which the distortion is very tiny on the blades of the fan
- The parameter that most improved the performance of the rotor is the *cp*, because it increase the polytropic efficiency up to 5e-3 with respect of the baseline
- The predictors that is more useful to optimized is the DC_{60} rather than the α, because it is able to reduce more the losses and the distortion of the total pressure

Chapter 5

Conclusions

The aim of the thesis was to understand and to have a preliminary idea on which are the interactions between the S-duct intake and a transonic fan. At the beginning, the first step was the study and the validation of the model, by simulating the single chnnel with clean inlet conditions. It was simulated just the single channel, because, since the flow is not distorted, the flow field is simmetrical. The problem is, that it was impossible to think to simulate just a piece of the S-duct with a single channel dowststream of it, because the distortion differently affects the blades. Therefore, an ogive was created to simulate the full anulus and the results are presented in §3.4 and §3.5. Despite the numbers of the iteration are not as much as the single channel, the simulations are well carried out. At this point, the challenging step was to assemble the two components together and to calculate how the performance of the fan are affected by the distortion of the pressure combined with the swirl. For this reason, the entire speed line is simulated and the results are reported in Table 10 in order to compare them with the clean inlet simulation. As a matter of fact and as it could have been expected, the overall performance are deteriorated; the η_{is} is negatively affected in both of the conditions (near stall and near peak condition), in fact the losses of efficiency is of 0.025. Along with the simulations, the deterioration of the stall margin has not been registered, but in order to be more accurate, more simulations should be performed. Once the interaction between the two components is understood, another further step is made. In agreement with the work in [12], it was decided to implement an optimization process to reduce the total pressure distortion on the blades of the rotor. Doing so, it was agreed to minimize both the pressure recovery factor and the DC_{60}. The results presented in §4.5 depicts a high improvement in the polytropic efficiency (up to 5e-3), plus the best results is achieved with the individual with the best pressure recovery factor. Furthermore, a second process of optmization was set up, with again the *cp* as objective and the α (swirl) as well. The optimized geometries are even better than the baseline's overall performance (e.g. η_{is} is improved for all the individuals), but, still, they are lower with respect to the first optimization. Therefore, from the results achieved in this work, it is more convenient to set up an optimization process, to try to minimize the DC_{60}. For instance, the distortion is almost removed from the blades of the rotor (see Fig. 66) and this utterly helps the the improvement of the overall performance, even if the pressure profile is not uniform.

Ringraziamenti

Questa tesi conclude un ciclo della mia vita, impegnativo, ma che alla fine mi ha regalato molte soddisfazioni. Durante questo percorso, molte sono state le persone che mi hanno supportato e aiutato nei momenti di difficoltá di questi anni.
In primis volevo ringraziare il Prof. Ernesto Benini per la Sua disponibilitá che mi ha mostrato in questi mesi di tesi e per la possibilitá che mi ha offerto.
Ringrazio Dr. Timoleon Kipouros e Prof. Mark Savill, per avermi accolto a Cranfield e per avermi aiutato in questo periodo presso la loro struttura.
Ringrazio i miei genitori, Mauro e Francesca, che mi hanno sempre incoraggiato ad andare avanti, che mi hanno sempre aiutato e supportato in ogni mia decisione e nel momento del bisogno ci sono sempre stati.
Ringrazio i miei nonni Carlo, Cosimo e Lola che da lassú mi hanno sempre protetto e la nonna Fanny che sta aspettando questo momento con estrema ansia. Inoltre vorrei di ringraziare tutti i miei zii e cugini che mi hanno sempre incoraggiato in questo percorso.
Ringrazio la Giorgia, la Pati, dal momento che sei stata la persona che mi stata piú vicino in questo cammino e non solo. Sei riuscita sempre a darmi la forza per andare avanti, hai sempre portato pazienza per tutto e sei stata sempre presente in ogni momento. Grazie veramente di cuore, ti voglio bene.
Ringrazio loro, i miei due Davide. Non solo siete state due persone indispensabili, ma siete per me due fratelli veri e propri. Dalle gare con il Garelli agli interminabili viaggi in Clio, ho passato momenti indimenticabili e che mi porteró per sempre con me. Grazie.
Ringrazio inoltre tutti gli amici con i quali in questi anni ho passato dei momenti fantastici e pieni di gioia. Non vi nomino tutti per paura di dimenticarne qualcuno.
Last, but not least, I would like to thank the all family of Cranfield, that helped me during this four months. For all the lunch breaks we have done together at CSA, for all the dinners we had (and here a big thank you to Giulia and Diana), thank you for everything. Looking forward to see you in a while.

References

[1] Ali Ameri. Nasa rotor 37 cfd code validation glenn-ht code. In *47th AIAA Aerospace Sciences Meeting including The New Horizons Forum and Aerospace Exposition*, page 1060, 2009.

[2] Bernhard H Anderson, Henry D Baust, and Johan Agrell. Management of total pressure recovery, distortion and high cycle fatigue in compact air vehicle inlets. 2002.

[3] John David Anderson Jr. *Fundamentals of aerodynamics*. Tata McGraw-Hill Education, 2010.

[4] Ernesto Benini. Dispense del corso di progetto di macchine.

[5] Ernesto Benini. Dispense del corso di propulsione aerea.

[6] Ernesto Benini. *Propulsione Aerea*. Cleup, 2014.

[7] Roberto Biollo. Systematic investigation on swept and leaned transonic compressor rotor blades. 2008.

[8] Roberto Biollo and Ernesto Benini. State-of-art of transonic axial compressors, advances in gas turbine technology. *ISBN*, pages 978–953, 2011.

[9] Roberto Biollo and Ernesto Benini. Recent advances in transonic axial compressor aerodynamics. *Progress in Aerospace Sciences*, 56:1–18, 2013.

[10] S16 Turbine Engine Inlet Distortion Committee et al. A methodology for assessing inlet swirl distortion. *Society of Automotive Engineers, AIR5686*, pages 1–108, 2007.

[11] Kevin Brendan Cramer. *Design of a total pressure distortion generator for aircraft engine testing*. PhD thesis, Virginia Tech, 2002.

[12] Davide Dal Magro. Implementation of uncertainty management techniques in the design of s-ducts intakes. 2018.

[13] Alessio DAmbros, Timoleon Kipouros, Pavlos Zachos, Mark Savill, and Ernesto Benini. Computational design optimization for s-ducts. *Designs*, 2(4):36, 2018.

[14] Anne-Laure Delot and Richard Scharnhorst. A comparison of several cfd codes with experimental data in a diffusing s-duct. In *49th AIAA/ASME/SAE/ASEE Joint PropulsionConference*, page 3796. 2013.

[15] Ahmed F El-Sayed and Mohamed S Emeara. Intake of aero-engines: A case study.

[16] Nicholas Fredrick and Milt Davis. Investigation of the effects of inlet swirl on compressor performance and operability using a modified parallel compressor model. In *ASME 2011 Turbo Expo: Turbine Technical Conference and Exposition*, pages 177–187. American Society of Mechanical Engineers, 2011.

[17] Abate Giada. Aerodynamic optimization of a transonic axial compressor rotor. 2012.

[18] Venturelli Giovanni. Development of numerical procedure for turbomachinery optimization. 2013.

[19] ANSYS Inc. Introduction to ansys fluent, turbulence modeling.

[20] H Kok, Mark Voskuijl, and Michel van Tooren. Distributed propulsion featuring boundary layer ingestion engines for the blended wing body subsonic transport. In *51st AIAA/ASME/ASCE/AHS/ASC Structures, Structural Dynamics, and Materials Conference 18th AIAA/ASME/AHS Adaptive Structures Conference 12th*, page 3064, 2010.

[21] Ahad Mehdi. Effect of swirl distortion on gas turbine operability. 2014.

[22] Kypros Milidonis, Bernhard Semlitsch, and Tom Hynes. Effect of clocking on compressor noise generation. *AIAA Journal*, 56(11):4225–4231, 2018.

[23] A Naseri, M Boroomand, and S Sammak. Numerical investigation of effect of inlet swirl and total-pressure distortion on performance and stability of an axial transonic compressor. *Journal of Thermal Science*, 25(6):501–510, 2016.

[24] James H Page, Paul Hield, and Paul G Tucker. Effect of inlet distortion features on transonic fan rotor stall. *Journal of Turbomachinery*, 140(7):071008, 2018.

[25] James H Page, Paul Hield, and Paul G Tucker. Effect of inlet distortion features on transonic fan rotor stall. *Journal of Turbomachinery*, 140(7):071008, 2018.

[26] Anthony J Strazisar, Jerry R Wood, Michael D Hathaway, and Kenneth L Suder. Laser anemometer measurements in a transonic axial-flow fan rotor. 1989.

[27] Kenneth L Suder. Blockage development in a transonic, axial compressor rotor. In *ASME 1997 International Gas Turbine and Aeroengine Congress and Exhibition*, pages V001T03A059–V001T03A059. American Society of Mechanical Engineers, 1997.